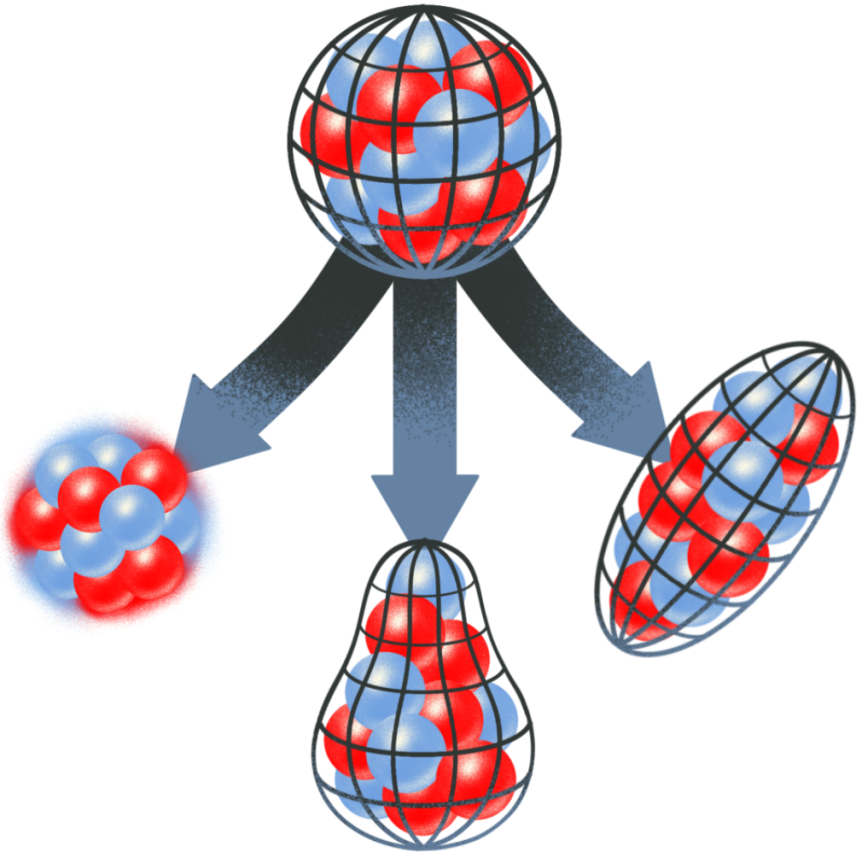

Symmetry-Projected Hartree-Fock-Bogoliubov Emulation

For Nuclear Systems with Parameter-Dependent Hamiltonians

Master's thesis in Physics

KELMEND MURIQI

DEPARTMENT OF PHYSICS AND ASTRONOMY

CHALMERS UNIVERSITY OF TECHNOLOGY

Gothenburg, Sweden 2026

www.chalmers.se

Master's thesis 2026

Symmetry-Projected Hartree-Fock-Bogoliubov Emulation

For Nuclear Systems with Parameter-Dependent Hamiltonians

Kelmend Muriqi

CHALMERS
UNIVERSITY OF TECHNOLOGY

Department of Physics and Astronomy
Division of Subatomic, High-Energy, and Plasma Physics
Theoretical Subatomic Physics
Chalmers University of Technology
Gothenburg, Sweden 2026

Symmetry-Projected Hartree-Fock-Bogoliubov Emulation

For Nuclear Systems with Parameter-Dependent Hamiltonians

Kelmend Muriqi

Supervisor: Christian Forssén and Alberto Scalesi, Department of Physics and Astronomy
Examiner: Christian Forssén, Department of Physics and Astronomy

Master's Thesis 2026
Department of Physics and Astronomy
Division of Subatomic, High-Energy, and Plasma Physics
Theoretical Subatomic Physics
Chalmers University of Technology
SE-412 96 Gothenburg
Telephone: +46 31 772 1000

Cover: Typical depictions of spherical, axial and octupolar nuclei, along with an interpretation of a superfluid nucleus. Illustrated by Vivien Dumm.

Typeset in LaTeX
Printed by Chalmers Digital Printing
Gothenburg, Sweden 2026

Symmetry-Projected Hartree-Fock-Bogoliubov Emulation
Kelmend Muriqi
Department of Physics and Astronomy
Chalmers University of Technology

Abstract

Nuclear systems consist of strongly interacting protons and neutrons. The general structure of these many-body systems can often be described by the nuclear shell model. The shell model predicts that there are certain nucleon numbers, referred to as magic numbers, which result in particularly stable configurations. These configurations are well described by spherical mean-field methods such as Hartree-Fock. Nuclei that are singly or doubly non-magic may, however, exhibit emergent deformations or pairing correlations, making the typical spherical mean-field approach insufficient. Deformations are conveniently captured by allowing the mean-field solutions to break rotational and/or parity symmetries. Pairing correlations are incorporated with the Hartree-Fock-Bogoliubov method, which employs Bogoliubov quasiparticles that potentially break particle number conservation. The broken symmetries must be restored to obtain physical states with good quantum numbers and to accurately calculate certain observables.

Contemporary models of the nuclear Hamiltonian are based on chiral effective field theory and involve free parameters referred to as low-energy constants. Exploring the continuous parameter space of these interaction models becomes computationally expensive with Hartree-Fock or Hartree-Fock-Bogoliubov solvers. The purpose of this project is to develop Eigenvector Continuation emulators for symmetry-breaking and symmetry-restored states, to approximate ground-state energies at a significantly reduced computational cost. In this work we vary only the C_{1S_0} low-energy constant, and thus explore a one-dimensional parameter space. We find that our emulators perform well using only three to six training points. For example, interpolation of the ^{18}O ground-state energy with restored particle number gives ~ 0.7 MeV error on average within an output energy range of approximately 400 MeV. Emulators constructed from states with broken angular momentum (without restoration) perform similarly, giving ~ 0.7 MeV errors on average. In conclusion, emulators can accurately reproduce Hartree-Fock-Bogoliubov ground-state energies before and after symmetry restoration with errors on the order of 1 MeV for nuclear systems with mass number ≈ 20.

Keywords: Nuclear Systems, Hartree-Fock, Deformations, Pairing, Bogoliubov, Symmetry Restoration, Eigenvector Continuation, Emulator.

Acknowledgements

I want to thank my supervisors, Prof. Christian Forssén and Dr. Alberto Scalesi for their guidance throughout this project. I have learned a whole lot from them and for that I am grateful.

I would like to thank the Theoretical Subatomic Physics group for the interesting discussions and inspiring presentations.

I want to thank my family for pushing me and being supportive of my choices.

Lastly, I want to thank Vivien for always being there for me in times of need.

Kelmend Muriqi, Gothenburg, June 2026

Table of contents

List of figures

List of tables

Acronyms

EC	eigenvector continuation. 3, 4, 25, 26, 37, 38
HF	Hartree-Fock. ix, xi, 1–4, 7–13, 16, 21, 22, 26, 33, 37
HFB	Hartree-Fock-Bogoliubov. ix, xi, 1–4, 10–14, 15, 16, 18, 19, 21–23, 25, 26, 28–35, 37
HO	harmonic oscillator. 6, 8, 18
LEC	low-energy constant. 3, 4, 25, 26, 28, 35, 38
PAV	projection after variation. xi, 2, 3, 21, 22
VAP	variation after projection. 2, 21

1. Introduction

Atomic nuclei consist of strongly interacting protons and neutrons. The structure of nuclei can be modeled using the nuclear shell model, in which nucleons occupy single-particle orbitals characterized by a set of quantum numbers [1]. In the shell model, nucleon energies appear in the form of discrete energy levels, known as shells. For some shells, the energy gap to the next is unusually large, making it especially energetically unfavorable for a nucleon to occupy the next. This leads to particularly stable configurations at certain nucleon numbers, known as magic numbers. The first magic numbers are

$$N, Z = 2, 8, 20, 28, 50, 82, 126. \tag{1.1}$$

Nuclei with these proton and neutron numbers are referred to as having closed shells. Note that a nuclear system could have zero, one, or two closed shells.

Accurate and precise modeling of nuclei is relevant for calculating observables and predicting the limit of stability [2]. Experimental data obtained via atomic mass evaluation [3] is limited to nuclei with sufficiently long lifetimes to perform physical measurements on, as shown in Figure 1.1. Exact calculations are feasible only for few-body systems, as the computational complexity increases exponentially with the number of nucleons [4].

Mean-Field Methods

In quantum many-body physics, there are several methods that address the problem of exponential scaling, such as In-Medium Similarity Renormalization Group, Coupled Cluster, and Many-Body Perturbation Theory [4]. These methods scale polynomially with the number of nucleons, and they start from a reference state. This is usually a mean-field solution found through Hartree-Fock (HF) or Hartree-Fock-Bogoliubov (HFB) solvers. In this project we specifically investigate the mean-field approaches.

The HF method is suited for the modeling of approximately spherical nuclei, often corresponding to closed-shell nuclei. In contrast, many open-shell nuclei exhibit emergent deformations, rendering spherical mean-field methods non-viable [6, 7]. Deformations are incorporated by allowing the intrinsic state to break rotational symmetry. This broken symmetry is reflected in the nucleon density distribution within the body-fixed frame.

Open-shell nuclei can also exhibit pairing correlations through the formation of Cooper pairs mediated by the nuclear force [8]. This is analogous to Cooper pairs formed between electrons, where the interaction is mediated by phonons. Bardeen-Cooper-Schrieffer theory states that pairing correlations can be modeled within a

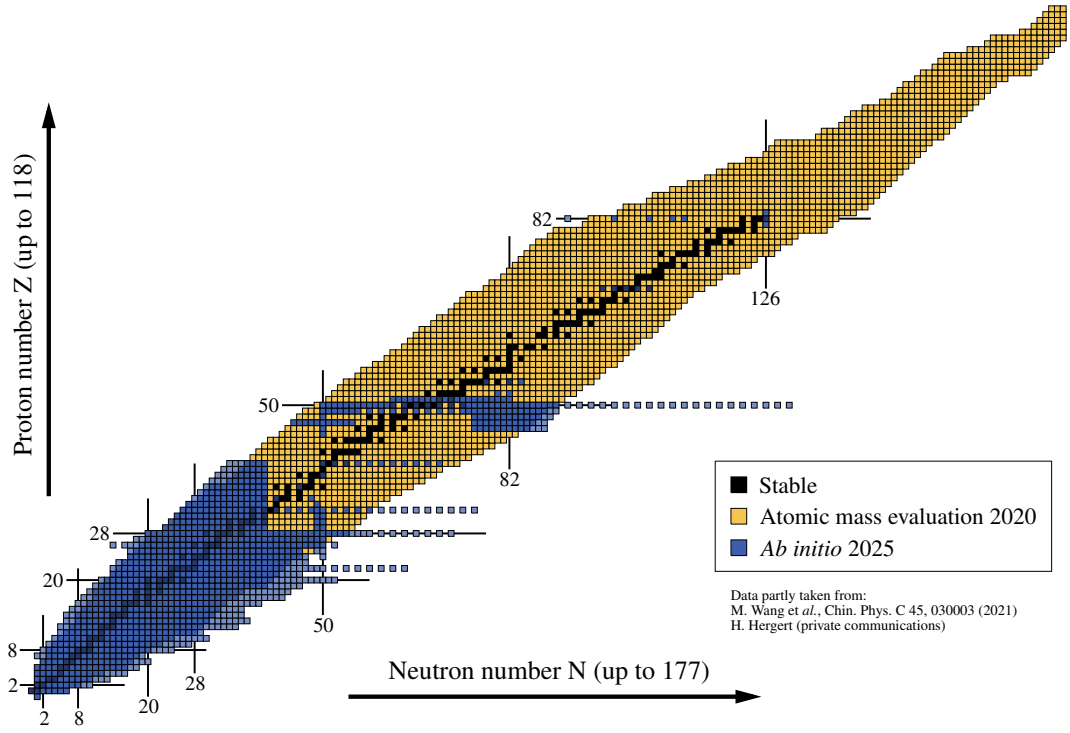

Figure 1.1: A nuclear chart showing the extent of experimental measurements (Atomic mass evaluation). For ab initio approaches there is no strict criterion: "all nuclei for which a *reasonable* calculation has been published" [5]. Taken from [5], courtesy of B. Bally.

mean-field picture by introducing the Bogoliubov quasi-particle basis [9]. In this basis, the particle number is not conserved, which is not a problem in condensed-matter systems with the approximately infinite atomic lattice. For nuclei, however, the particle number must be constrained to be in average the one of the physical system. The conservation of the average particle number is achieved by a tunable Lagrange multiplier [8].

HFB unifies HF and Bardeen-Cooper-Schrieffer theory, capturing pairing correlations and deformations [8]. As mentioned, the deformation is conveniently described by breaking of rotational symmetry, specifically not conserving the quantum numbers angular momentum and parity [7]. The change of basis to Bogoliubov quasiparticles can lead to breaking of particle number. The physical state can not break any of these symmetries. Therefore, when calculating observables, these quantities must be conserved, meaning that the broken symmetries must be restored.

Incorporating the restoration of symmetries in the HFB calculations can be achieved in two different ways. During the variational calculation, one may restore the symmetry at each iteration step, named variation after projection (VAP) [10]. The other option is to restore the symmetries only after finding the symmetry-broken variational solution, called projection after variation (PAV) [7]. PAV is the simpler and cheaper approach, whereas VAP will lead to a more accurate result including

more correlations.

Emulators

Certain interactions described by the nuclear Hamiltonian are parametrized [2, 6, 11]. The Hamiltonian is constructed through systematic expansion of nuclear and electroweak forces with chiral effective field theory [12]. The long-range interactions such as the Coulomb interaction and those governed by pion exchanges are treated explicitly, but the short-range parts are given by a set of contact interactions with strengths governed by coupling constants referred to as low-energy constants (LECs). The Hamiltonian can be written as

$$H = H_0 + \sum_i x_i H_i, \tag{1.2}$$

where H_0 contains constant terms and H_i is the short-range part corresponding to the LEC x_i. Typically the LEC values are fitted such that the interaction model can reproduce low-energy two-nucleon scattering data.

A typical parametrization of the Hamiltonian includes a total of 17 LECs [2]. A ground-state calculation of a single point in the continuous parameter space can take minutes or hours with HF or HFB. The high computational cost makes LEC sensitivity studies unpractical. Therefore, it is convenient to employ some sort of emulation or surrogate model.

Emulators using eigenvector continuation (EC) are well-fit for studying the space of LECs [13]. EC constructs a low-dimensional basis spanned by eigenvectors generated from a small set of different parameter points. This reduced basis model is used to approximate solutions at new parameter values. In this case, the parameters are the LECs, and the eigenvectors are the ground states of a specific nucleus. Emulators allow for accurate interpolation and even extrapolation of observables.

In previous works, emulators have been constructed with HF on closed shell [11] and axially-deformed nuclei, the latter along with restoration of angular momentum [6]. However, closed-shell and axially-deformed nuclei only constitute a subset of all observations. Developing an EC emulator for HFB or octupole deformed states would enable analysis of many more nuclear systems.

Specific aim

The goal of this project is to develop an HFB emulator framework that employs EC along with projection of symmetries. The exact objectives are:

- Implement PAV for restoration of particle number, angular momentum, and parity on HFB states.
- Develop and construct HFB emulators using EC on different nuclei.
- Analyze the performance of the emulators.

Limitations

The first limitation concerns nuclear mass number. The variational computation can become expensive for heavier nuclei. For this project nuclear systems with mass number ≈ 20 will be analyzed. Furthermore, the proton and neutron numbers will always be even for all calculations.

When it comes to analyzing the performance of the emulators there are some further limitations. Emulation of HFB has never been extensively explored, so these emulators will also be compared to previous HF emulators with the expected result being a slightly worse performance due to higher complexity.

Another limitation concerns how many of these symmetries are projected at the same time. For this thesis, only one symmetry will be projected at a time. This is purely due to how much time is available, but a natural next step would be to extend the framework to restore multiple symmetries at once.

Lastly, we make the choice of varying only one LEC. The chosen LEC is $C_{^1S_0}$ which is expected to have the highest impact on ground state energies.

Structure

This thesis is divided into three main chapters containing theory, method, results, and discussions. Chapter 2 will introduce basic many-body formalism and the theory behind the HF and HFB methods. Chapter 3 contains the theory and implementation of the projection operators, including selected results for calculated observables. Chapter 4 describes the development of the EC emulators.

We end with a brief summary and conclusive statements in Chapter 5, along with suggestions for improvements and future work.

2. Many-Body Physics

We start this chapter by reviewing the quantum many-body formalism. Later we introduce the mean-field methods used in this project. In the end we present ground-state energy calculations where the intrinsic state may or may not break symmetries of the Hamiltonian.

2.1 Slater Determinants

Let us quickly remind ourselves of symmetric and antisymmetric states. A symmetric two-particle state is defined as

$$|\Psi_\mathrm{s}\rangle = \frac{1}{\sqrt{2}} \left(|\psi_1\rangle \, |\psi_2\rangle + |\psi_2\rangle \, |\psi_1\rangle \right), \tag{2.1}$$

where we have the particle 1 and particle 2 states. Clearly, under the permutation of the two particles the permuted state remains exactly the same since we get

$$|\Psi'_\mathrm{s}\rangle = \frac{1}{\sqrt{2}} (|\psi_2\rangle \, |\psi_1\rangle + |\psi_1\rangle \, |\psi_2\rangle) \tag{2.2}$$

$$\implies |\Psi'_\mathrm{s}\rangle = |\Psi_\mathrm{s}\rangle \, . \tag{2.3}$$

An antisymmetric two-particle state reads

$$|\Psi\rangle = \frac{1}{\sqrt{2}} (|\psi_1\rangle \, |\psi_2\rangle - |\psi_2\rangle \, |\psi_1\rangle), \tag{2.4}$$

which under the exchange of the two particles

$$|\Psi\rangle = - \, |\Psi'\rangle \, . \tag{2.5}$$

Antisymmetric states are of primary interest here, as they describe fermionic systems, such as many-nucleon states.

The state in equation (2.4) can be written as a determinant [14]

$$|\Psi\rangle = \frac{1}{\sqrt{2}} \begin{vmatrix} |\psi_1\rangle & |\psi_2\rangle \\ |\psi_1\rangle & |\psi_2\rangle \end{vmatrix}. \tag{2.6}$$

This form for expressing an antisymmetric state is known as a Slater determinant [14]. The general expression for a many-body state in an independent-particle picture is

$$|\Psi\rangle = \frac{1}{\sqrt{A}} \begin{vmatrix} |\psi_1\rangle & |\psi_2\rangle & \cdots & |\psi_A\rangle \\ |\psi_1\rangle & |\psi_2\rangle & \cdots & |\psi_A\rangle \\ \vdots & \vdots & \ddots & \vdots \\ |\psi_1\rangle & |\psi_2\rangle & \cdots & |\psi_A\rangle \end{vmatrix}, \tag{2.7}$$

where A is the number of fermions.

A more powerful way of expressing many-body states is through second quantization; a formalism in quantum mechanics in which particles are described by creation and annihilation operators acting on occupation-number states. The fermionic creation(annihilation) operator $c_k^\dagger(c_k)$ creates(removes) a particle in state k. The operators $c_k^\dagger, c_k$ encode antisymmetry through the anticommutation relations [15]

$$\{c_k^\dagger, c_l^\dagger\} = 0, \{c_k, c_l\} = 0 \tag{2.8}$$

$$\{c_k^\dagger, c_l\} = \delta_{kl}. \tag{2.9}$$

Using these operators, a Slater determinant can be expressed as

$$|\Psi\rangle = \prod_k (c_k^\dagger)^{n_k} |0\rangle \,, \tag{2.10}$$

with $n_k \in \{0, 1\}$ being the occupation number of single-particle state k, and $|0\rangle$ being the vacuum. Occupied single-particle states are often referred to as *holes* whereas unoccupied states are referred to as *particles*.

2.2 The Model Space

In nuclear physics, the harmonic oscillator (HO) basis provides a convenient representation of single-particle states. With the HO basis the individual orbitals are defined by the following set of quantum numbers [10]

$$|i\rangle \equiv |t_i \, j_i \, m_i \, l_i \, n_i\rangle \tag{2.11}$$

where the variables t, j, m, l, n each correspond to the quantities shown below

$$\begin{aligned} t &\rightarrow \text{Isospin} \\ j &\rightarrow \text{Total angular momentum} \\ m &\rightarrow \text{Magnetic number} \\ l &\rightarrow \text{Orbital angular momentum} \\ n &\rightarrow \text{Radial quantum number.} \end{aligned}$$

The list of all single-particle states employed in the many-body calculation is called the model space. In principle, the model space is infinite but in practice it must be truncated.

The energy levels are defined by the radial quantum number n and the orbital angular momentum l as [16]

$$E = (2n + l + \frac{3}{2})\hbar\omega = (e + \frac{3}{2})\hbar\omega, \tag{2.12}$$

where ω is the oscillator frequency. The truncation of the model space is achieved by limiting the maximum energy of single-particle states as

$$2n + l \leq e_{\max}. \tag{2.13}$$

Due to this truncation, the choice of oscillator frequency ω affects the convergence of the calculation and should be optimized to minimize the energy. Throughout this project, the oscillator frequency is fixed to $\hbar\omega = 20$ MeV, because for HF (introduced in section 2.3) it is the value that gives the lowest energy for the nuclei and interaction of interest.

We realize that filling the basis states with the lowest single-particle energies does not necessarily correspond to the many-body ground state due to interactions between single-particle states [8]. To find the Slater determinant that best represents the ground state, a unitary transformation is necessary to express each single particle orbital as a superposition (linear combination) of the basis states as [8]

$$|\psi_j\rangle = \sum_i C_{ij} |i\rangle , \tag{2.14}$$

where C the matrix of coefficients defining the linear combination. What ends up becoming the variational problem of finding the ground state, is finding the coefficient matrix C that minimizes the energy of the many-body system. The other option, which is more complicated, is to find a more general solution in the form of a superposition of Slater determinants [8]:

$$|\Phi\rangle = \sum_i a_i |\Psi_i\rangle , \tag{2.15}$$

where $|\Phi\rangle$ is a many-body state, but not a single Slater determinant.

2.3 Hartree-Fock

The HF method is a well known mean-field method for finding an approximated ground state of an atomic nucleus. The idea is to find the one-body density matrix [8]

$$\rho_{kl} = \langle\Psi| c_l^\dagger c_k |\Psi\rangle , \tag{2.16}$$

such that the energy functional

$$E[\Psi] = \frac{\langle\Psi| H |\Psi\rangle}{\langle\Psi|\Psi\rangle} = \frac{\langle\Psi| T + V |\Psi\rangle}{\langle\Psi|\Psi\rangle} \tag{2.17}$$

$$E[\rho] = \sum_{pq} t_{pq}\rho_{qp} + \frac{1}{2}\sum_{pqrs} \rho_{rp} v_{pqrs} \rho_{sq}, \tag{2.18}$$

is minimized. Note that T and V denote the kinetic energy and the two-body interactions of the Hamiltonian, respectively, typically specified by chiral effective field theory [12]. t_{pq} and v_{pqrs} are the matrix elements of T and V. The indices p, q, r, s correspond to single-particle basis states.

As mentioned, the HF method minimizes the energy functional with respect to ρ, and to perform this minimization we consider a variation $\delta\rho$. The variation of the energy can then be written as [8]

$$\delta E = E[\rho + \delta\rho] - E[\rho] \approx \sum_{pq} \frac{\partial E^{\mathrm{HF}}[\rho]}{\partial \rho_{qp}} \delta\rho_{qp}. \tag{2.19}$$

We can define the matrix elements of the HF single-particle Hamiltonian as [8]

$$h_{pq} = \frac{\partial E^{\mathrm{HF}}[\rho]}{\partial \rho_{qp}} = t_{pq} + \sum_{rs} v_{prqs}\rho_{sr} = t_{pq} + \Gamma_{pq}. \tag{2.20}$$

However, not all variations of the density matrix are allowed, as they are limited by the constraint [8]

$$(\rho + \delta\rho)^2 = \rho + \delta\rho, \tag{2.21}$$

due to the idempotency requirement $\rho^2 = \rho$. The constraint expanded up to linear terms is

$$\delta\rho = \rho\delta\rho + \delta\rho\rho. \tag{2.22}$$

The above means that if a diagonal ρ matrix is found with eigenvalues 1 or 0, the only allowed variations are the particle-hole elements in the density matrix resulting in a block-off-diagonal $\delta\rho$. A diagonal ρ results in a block-diagonal HF Hamiltonian h, separating particle and hole subspaces, and thus [8]

$$\delta E = \sum_{pq} h_{pq}\,\delta\rho_{qp} = 0. \tag{2.23}$$

In practice, the minimization can be solved iteratively as follows.

- Step 0: Make an initial guess for the one-body density matrix $\rho^{(0)}$.
- Step 1: Construct the mean-field Hamiltonian and solve the eigenvalue equation

  $$h[\rho^{(0)}]\,|\psi_j\rangle = \varepsilon_j\,|\psi_j\rangle\,, \tag{2.24}$$

  where ε_j is the single-particle energy of orbital $|\psi_j\rangle$. The above can be expressed in the HO basis with the coefficient matrix as

  $$h[\rho^{(0)}]C = \mathrm{diag}(\vec{\varepsilon})\,C. \tag{2.25}$$

- Step 2: Construct the new density from the orbitals

  $$\rho^{(1)} = \sum_{j\in\mathrm{occ}} |\psi_j\rangle\,\langle\psi_j|\,, \tag{2.26}$$

  or in the HO basis

  $$\rho^{(1)}_{kl} = \sum_{j\in\mathrm{occ}} C_{kj}C^*_{lj}. \tag{2.27}$$

- Step 3: Check convergence by comparing the densities (or energies)

  $$||\rho^{(1)} - \rho^{(0)}|| < \epsilon_\rho, \quad \left(|E[\rho^{(0)}] - E[\rho^{(1)}]| < \epsilon_E\right), \tag{2.28}$$

  where ϵ is a small tolerance parameter. If the criterion above has been reached, then the ground state is found. If not, set the new guess for the density $\rho^{(0)} = \rho^{(1)}$ and repeat steps $1-3$.

The following results are from an HF-solver developed by Alberto Scalesi [17]. A nucleus like ^{16}O is doubly magic ($N = 8, Z = 8$), making spherical HF well suited for its mean-field description. Table 2.1 shows the calculated spherical HF energies for ^{16}O, ^{18}O, and ^{20}Ne with truncation $e_{\max} = 8$. The used Hamiltonian model is called NNLO$_{\text{go}}$(394) [18].

Table 2.1: Ground state energy calculations with spherical HF for three different nuclei.

Nucleus	^{16}O	^{18}O	^{20}Ne
HF-Energy [MeV]	-146.855	-160.901	-176.739

We will realize that allowing ^{16}O to break symmetries, as discussed in the next section, will not have an effect on its calculated energy. For other cases though, like ^{18}O and ^{20}Ne, there exists a lower energy configuration that cannot be found through spherical HF.

2.4 Broken Symmetries

Because the HF Hamiltonian h is not only dependent on the original Hamiltonian, but also the density ρ, it does not necessarily have the same symmetries as the original Hamiltonian. This is reflected in the solution having one or more broken symmetries. The breaking of symmetries allows for approximate incorporation of many-body correlations while still remaining in the independent-particle picture [8]. The concerned symmetries are rotations, parity, and particle number. In this section we discuss mainly rotations and parity, whereas the framework used for breaking of particle number is discussed in section 2.5.

In HF theory there are certain conserved symmetries referred to as the self-consistent symmetries. For any matrix S corresponding to a symmetry operator

$$\hat{S} = \sum_{kk'} S_{kk'} c_k^\dagger c_{k'}, \tag{2.29}$$

that commutes with the Hamiltonian

$$[H, \hat{S}] = 0, \tag{2.30}$$

the field h has the property

$$Sh[\rho]S^\dagger = h[S\rho S^\dagger]. \tag{2.31}$$

This means that if $\rho^{(0)}$ has a symmetry S, then so does $h[\rho^{(0)}]$ [8]. Because $\rho^{(1)}$ is constructed by diagonalizing $h[\rho^{(0)}]$ it also preserves the symmetry. The consequence is that if the initial density $\rho^{(0)}$ has a certain symmetry, then so does the solution.

However, in practical HF calculations tiny perturbations in the form of numerical errors can accumulate [8]. If the symmetry-preserving solution is stable in the full variational space, then the tiny errors decay. However, if the solution is not a local minimum in the full space, then the perturbations grow over iterations, resulting in a symmetry-broken solution. This means that starting with a spherical initial density $\rho^{(0)}$ could still lead to a deformed solution if that is energetically favorable.

2.5 Quasiparticles and Bogoliubov Theory

Certain nuclei with partially filled shells exhibit pairing correlations through the formation of Cooper pairs. The pairing correlations can be captured within a single-particle picture by introducing the Bogoliubov quasiparticle basis. The quasiparticle creation and annihilation operators are defined as [8]

$$\beta_k^\dagger = \sum_l \left(U_{lk}\ c_l^\dagger + V_{lk}\ c_l \right) \tag{2.32}$$

$$\beta_k = \sum_l \left(U_{lk}^*\ c_l + V_{lk}^*\ c_l^\dagger \right), \tag{2.33}$$

where U and V are matrices of coefficients. Using this change of basis and working with the same principles as HF leads to the HFB method. The introduction of the Bogoliubov quasiparticles leads to broken particle-number symmetry.

In the case of nuclei, the particle number is an important defining part of the system. In order to obtain a realistic description of the system we conserve the average particle number. This is achieved by adding a Lagrange multiplier λ term to the Hamiltonian [8]

$$H' = H - \lambda \hat{N}. \tag{2.34}$$

The Lagrange multiplier λ is tuned such that the average particle number is that of the physical system N

$$\langle \hat{N} \rangle = N. \tag{2.35}$$

Let us introduce the HFB vacuum $|\Phi\rangle$ defined as the state that is annihilated by the quasiparticle annihilation operator [8]

$$\beta_k \left| \Phi \right\rangle = 0. \tag{2.36}$$

Due to the change of basis, the extra degree of freedom that allows for breaking of particle number results in the HFB vacuum being a superposition of Slater determinants with good particle number [8]

$$|\Phi\rangle = \sum_k g_{N_k}\ |\Psi^{N_k}\rangle\,, \tag{2.37}$$

where g_{N_k} is the weight corresponding to the state with particle number N_k.

With the HFB vacuum we can introduce the normal density matrix ρ along with the anomalous density matrix κ

$$\rho_{kl} = \langle \Phi | \, c_l^\dagger \, c_k \, | \Phi \rangle \,, \qquad \kappa_{kl} = \langle \Phi | \, c_l \, c_k \, | \Phi \rangle \,, \tag{2.38}$$

or expressed with the coefficient matrices

$$\rho = V^* V^{\mathrm{T}}, \qquad \kappa = V^* U^{\mathrm{T}}. \tag{2.39}$$

Starting from κ, we can introduce the pairing field

$$\Delta_{pq} = \frac{1}{2} \sum_{rs} v_{pqrs} \kappa_{rs}, \tag{2.40}$$

and the HF Hamiltonian

$$h = t + \Gamma - \lambda I, \tag{2.41}$$

where I is the identity matrix.

The fields introduced above appear in the HFB equations [8]

$$\begin{pmatrix} h & \Delta \\ -\Delta^* & -h^* \end{pmatrix} \begin{pmatrix} U_k \\ V_k \end{pmatrix} = \begin{pmatrix} U_k \\ V_k \end{pmatrix} E_k, \tag{2.42}$$

where E_k is the energy of quasiparticle state k. These equations can also be solved until self-consistency is reached, except now the energy functional to be minimized is [8]

$$E[\rho, \kappa] = \sum_{pq} t_{pq} \rho_{qp} + \frac{1}{2} \sum_{pqrs} \rho_{rp} v_{pqrs} \rho_{sq} + \frac{1}{4} \sum_{pqrs} \kappa^*_{pq} v_{pqrs} \kappa_{rs}, \tag{2.43}$$

leading to equation (2.42). However, with a larger and more complicated system of equations, one might want to use a more convenient way of finding the ground state energy than the self-consistent method.

2.6 The Gradient Method

In both HF and HFB, self-consistently solving the eigenvalue equation can be unstable and convergence is not guaranteed [8]. One issue that may arise is that the iterative solutions oscillate around the ground state without converging to it as shown in Figure 2.1. A more reliable way of reaching convergence is the gradient method [8, 10].

The gradient method works by taking a step towards the steepest descent of energy in each iteration. Let us express the Hamiltonian in terms of the quasiparticle operators

$$H = H^0 + \sum_{k_1 k_2} H^{11}_{k_1 k_2} \beta^\dagger_{k_1} \beta_{k_2} + \sum_{k_1 < k_2} \left(H^{20}_{k_1 k_2} \beta^\dagger_{k_1} \beta^\dagger_{k_2} + \text{h.c.} \right) + \ldots, \tag{2.44}$$

where the dots indicate interaction terms, and H^{ij} is a prefactor for the term with i creation operators and j annihilation operators. We also introduce the theorem of

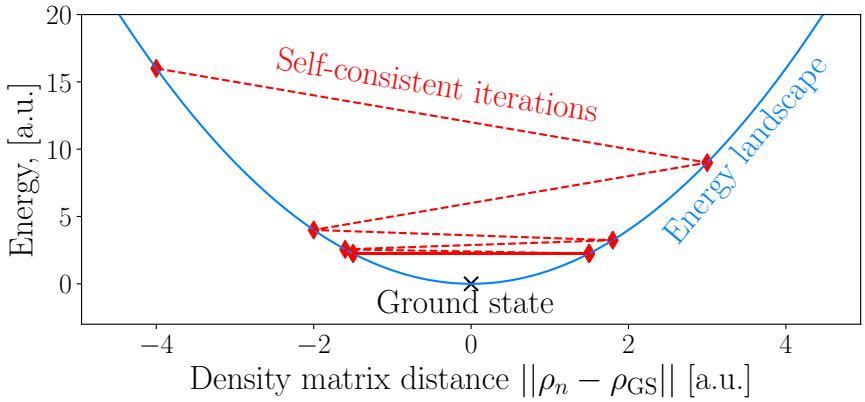

Figure 2.1: Shows how trying to solve the HF or HFB equations self-consistently could lead to oscillations around the ground state.

Thouless, which states that an HFB state can be rotated into another HFB state that is not orthogonal to the original one as follows [8, 19]

$$|\Phi'\rangle = \exp\left(\sum_{k_1<k_2} Z_{k_1k_2}\beta^\dagger_{k_1}\beta^\dagger_{k_2}\right)|\Phi\rangle\,. \tag{2.45}$$

With this, the energy may be expressed as

$$E(Z) = \frac{\langle\Phi'|\,H\,|\Phi'\rangle}{\langle\Phi'|\Phi'\rangle} = H^0 + \begin{pmatrix} H^{20*}, & H^{20}\end{pmatrix}\begin{pmatrix} Z \\ Z^*\end{pmatrix} + \dots \tag{2.46}$$

Starting with the HFB state $|\Phi_0\rangle$, the goal is to rotate to the state $|\Phi_1\rangle$, which corresponds to a step towards the steepest descent in energy. The coefficients $Z_{1k_1k_2}$ are chosen as the negative derivative of the energy [8, 10]

$$Z_{1k_1k_2} = -\eta\frac{\partial}{\partial Z^*_{k_1k_2}}E(Z)\bigg|_{Z=0} = -\eta H^{20}_{k_1k_2}, \tag{2.47}$$

where η is a parameter deciding the size of the step. Note that this is also an iterative method, and it uses the same convergence criterion as the self-consistent method for HF.

2.7 Ground-state Results

All the results in table 2.2 are calculated with an HF/HFB solver developed by Alberto Scalesi [17]. In these results the truncation is $e_{\max} = 8$ and the interaction is $\text{NNLO}_{\text{go}}(394)$. The different methods discussed until now are used, which we refer to as:

- Spherical HF → conserves all symmetries.
- Axial HF → can break angular momentum symmetry.

- Spherical HFB → can break particle number symmetry.
- Axial HFB → can break angular momentum and particle number symmetry.

Axial HFB allows for the inclusion of the largest amount of correlations, therefore it should always result in the lowest energy. The investigated nuclei are ^{16}O, ^{18}O, and ^{20}Ne.

In table 2.2 the energy for ^{16}O remains the same even though more symmetries are allowed to be broken. These results greatly suggest that the lowest-energy solution for ^{16}O does not break particle number or angular momentum.

Looking a bit deeper into ^{18}O, the energy is slightly lower for axial HF than for spherical HF, but the lowest is found at spherical or axial HFB. The fact that we see a lower energy for axial HF than for spherical tells us that if we conserve particle number, there exists a lower-energy configuration with broken angular momentum. Because spherical HFB and axial HFB result in the same energy, we may deduce that the lowest-energy configuration breaks particle number but not angular momentum.

For ^{20}Ne we find the lowest energies when using axial HF and axial HFB. Using the same logic here, it is clear that the lowest-energy configuration of ^{20}Ne breaks angular momentum but not particle number.

Table 2.2: Ground state energy calculations for three different nuclei with different methods. The symbols stand for spherical (∘) and axial (⬭).

Nucleus	^{16}O	^{18}O	^{20}Ne
∘ HF [MeV]	-146.855	-160.901	-176.739
⬭ HF [MeV]	-146.855	-161.785	-187.698
∘ HFB [MeV]	-146.855	-162.787	-177.764
⬭ HFB [MeV]	-146.855	-162.787	-187.698

Though our observations are consistent with what one would expect for these nuclei, we may also calculate some different parameters that inform us of the degree of symmetry breaking. These parameters are the variance of the particle number Var$[\hat{N}]$ and the measure of rotational symmetry breaking β_2, defined in appendix A. Table 2.3 shows the calculated values of Var$[\hat{N}]$ and β_2 for the three nuclei after finding the ground state with axial HFB. It clearly shows that ^{18}O is breaking particle number, while ^{20}Ne is breaking angular momentum.

Table 2.3: Calculated diagnostic parameters. The underlying mean-field method is axial HFB.

Nucleus	^{16}O	^{18}O	^{20}Ne
Var$[\hat{N}]$	0.0	2.768	0.0
β_2	0.0	0.0	0.3155

3. Restoration of Symmetries

In the previous chapter, we explained how to incorporate certain nuclear correlations and deformations exhibited in open-shell nuclei. This led to broken symmetries like angular momentum and particle number. The symmetries need to be restored because physical states must have good quantum numbers to be comparable with experiments and to remove unphysical mixing. In this chapter we introduce the restoration of symmetries with symmetry projection operators.

3.1 Projection Operators

As mentioned, a general HFB state with broken symmetries can be written as a superposition of orthogonal states with good quantum numbers

$$|\Phi\rangle = \sum_k g_{S_k} |\Psi^{S_k}\rangle \,, \tag{3.1}$$

where S_k is an arbitrary quantum number. The projection operators, denoted $\hat{P}^{S_0}$, extracts one of these states as

$$\hat{P}^{S_0} |\Phi\rangle = g_{S_0} |\Psi^{S_0}\rangle \,. \tag{3.2}$$

The projected energy is calculated via [8]

$$E_{\text{proj}} = \frac{\langle\Phi| H \hat{P}^{S_0} |\Phi\rangle}{\langle\Phi| \hat{P}^{S_0} |\Phi\rangle}. \tag{3.3}$$

Now we will explain how a general symmetry projection operator is constructed. Each symmetry corresponds to a symmetry operator $\hat{S}$

$$\hat{S} |\Psi^{S_0}\rangle = S_0 |\Psi^{S_0}\rangle \,. \tag{3.4}$$

Continuous symmetry groups can be generated with its symmetry operator and the corresponding continuous angle Ω as [8]

$$\hat{R}(\Omega) = e^{i\Omega\hat{S}}. \tag{3.5}$$

The action of the symmetry operator on the HFB state gives

$$e^{i\Omega\hat{S}} |\Phi\rangle = \sum_k g_k e^{i\Omega\hat{S}} |\Psi^{S_k}\rangle \tag{3.6}$$

$$= \sum_k g_k e^{i\Omega S_k} |\Psi^{S_k}\rangle \tag{3.7}$$

A target quantum number S_0 can be chosen by multiplying with $e^{-i\Omega S_0}$ and integrating over the angle Ω

$$\int d\Omega\, e^{i\Omega(\hat{S}-S_0)} \left|\Phi\right\rangle = \sum_k g_k \int d\Omega\, e^{i\Omega(S_k-S_0)} \left|\Psi^{S_k}\right\rangle . \tag{3.8}$$

Note that the integral on the right-hand side is equal to zero when $S_k \neq S_0$, therefore we are left with

$$\int d\Omega\, e^{i\Omega(\hat{S}-S_0)} \left|\Phi\right\rangle = \sum_k 2\pi\delta_{k,0}\, g_k \left|\Psi^{S_k}\right\rangle \tag{3.9}$$

$$= 2\pi g_0 \left|\Psi^{S_0}\right\rangle . \tag{3.10}$$

We thus find the projection operator for a symmetry S [8]

$$\hat{P}^{S_0} = \frac{1}{2\pi} \int d\Omega\, e^{i\Omega(\hat{S}-S_0)}. \tag{3.11}$$

Projection operators are used to calculate symmetry-projected quantities. The projected norm and energy are calculated via [20]

$$|g_{S_0}|^2 = \left\langle\Phi\right| \hat{P}^{S_0} \left|\Phi\right\rangle = \frac{1}{2\pi} \int d\Omega\, e^{i\Omega S_0} \left\langle\Phi\right| \hat{R}(\Omega) \left|\Phi\right\rangle \tag{3.12}$$

$$E_{\text{proj}} = \frac{\left\langle\Phi\right| H\hat{P}^{S_0} \left|\Phi\right\rangle}{\left\langle\Phi\right| \hat{P}^{S_0} \left|\Phi\right\rangle} = \frac{1}{2\pi|g_{S_0}|^2} \int d\Omega\, e^{i\Omega S_0} \frac{\left\langle\Phi\right| H\hat{R} \left|\Phi\right\rangle}{\left\langle\Phi\right| \hat{R} \left|\Phi\right\rangle} \left\langle\Phi\right| \hat{R} \left|\Phi\right\rangle . \tag{3.13}$$

A way to calculate the overlap $\left\langle\Phi\right| \hat{R} \left|\Phi\right\rangle$ for a general rotation operator $\hat{R}$ and HFB state $\left|\Phi\right\rangle$ must be found.

3.2 Calculation of Overlap

For an HFB solution, we start by constructing and diagonalizing the density matrix $\rho = V^* V^{\mathrm{T}}$. This gives the eigenvectors D_k and eigenvalues v_k^2, which define the canonical basis [8]. These eigenvalues represent occupation probabilities $v_k^2 \in [0, 1]$, so we extract the eigenvectors corresponding to nonzero eigenvalues, denoted D_{occ}. The eigenvectors are used to calculate the matrix of overlaps

$$\mathcal{O} = D_{\text{occ}}^{\dagger} R D_{\text{occ}}, \tag{3.14}$$

to then calculate the determinant $\det(\mathcal{O})$ [10, 21]. For an HF state, this would conclude the calculation of the overlap, but because the occupation probabilities in HFB can be between 0 and 1, further handling is required.

The partially occupied orbitals are handled by extracting their eigenvalues and calculating the Pfaffian, explained in Appendix B, of a skew-symmetric matrix. In the canonical basis, we end up with pairs identified by degenerate eigenvalues and opposite values of the quantum number m [8, 21]. Particularly, if the pairs are ordered such that they are adjacent, we have

$$v_{2n}^2 = v_{2n+1}^2, \tag{3.15}$$

where n is an integer. These pairs are referred to as canonical pairs [8], and are used to construct the skew-symmetric matrix M [21]. Let us first express the elements that will enter the matrix as $m_k = v_k/\sqrt{1-v_k^2}$. For N partially occupied orbitals, the dimension of M is $2N \times 2N$. For a case with just one pair of partially occupied orbitals, the matrix is constructed as [21]

$$M = \begin{pmatrix} 0 & m_0 & & -\mathcal{O}_{\mathrm{p}}^{-1} \\ -m_0 & 0 & & \\ & & 0 & -m_0 \\ \mathcal{O}_{\mathrm{p}}^{-T} & & m_0 & 0 \end{pmatrix}, \tag{3.16}$$

where $\mathcal{O}_p$ is the sub-block of the overlap matrix corresponding only to partially occupied orbitals. The Pfaffian $\mathrm{pf}(M)$ is then calculated via an algorithm developed by M. Wimmer [22], and the final overlap is

$$\langle\Phi|\,\hat{R}\,|\Phi\rangle = \sigma\,\mathrm{pf}(M)\,\det(\mathcal{O}), \tag{3.17}$$

where σ is a sign factor.

3.3 Calculation of Energy Element

For the calculation of the energy element

$$E_\Omega = \frac{\langle\Phi|\,H\hat{R}(\Omega)\,|\Phi\rangle}{\langle\Phi|\,\hat{R}(\Omega)\,|\Phi\rangle}, \tag{3.18}$$

we start by defining the transition densities [10]

$$\rho_{ij}^{01} = \frac{\langle\Phi_0|\,c_j^\dagger c_i\,|\Phi_1\rangle}{\langle\Phi_0|\Phi_1\rangle} \tag{3.19}$$

$$\kappa_{ij}^{01} = \frac{\langle\Phi_0|\,c_j c_i\,|\Phi_1\rangle}{\langle\Phi_0|\Phi_1\rangle} \tag{3.20}$$

$$\kappa_{ij}^{10*} = \frac{\langle\Phi_0|\,c_i^\dagger c_j^\dagger\,|\Phi_1\rangle}{\langle\Phi_0|\Phi_1\rangle}, \tag{3.21}$$

where $|\Phi_1\rangle$ corresponds to the rotated state $\hat{R}\,|\Phi\rangle$ and $|\Phi_0\rangle$ to the unrotated state $|\Phi\rangle$. The transition densities expressed in terms of the U and V matrices are [10]

$$\rho^{01} = V_1^*(A^T)^{-1}V_0^T \tag{3.22}$$

$$\kappa^{01} = V_1^*(A^T)^{-1}U_0^T \tag{3.23}$$

$$\kappa^{10*} = V_0A^{-1}U_1^\dagger, \tag{3.24}$$

where $A = U_1^\dagger U_0 + V_1^\dagger V_0$.

The energy element is now calculated in a similar way as the energy functional introduced in equation (2.43). As used before, the matrix elements of the Hamiltonian operators can be expressed as a one-body part t and a two-body part v. The energy element becomes [10]

$$E_\Omega = \sum_{ij} t_{ij}\rho_{ji}^{01} + \frac{1}{2}\sum_{ijkl} v_{ijkl}\rho_{ki}^{01}\rho_{lj}^{01} + \frac{1}{4}\sum_{ijkl} v_{ijkl}\kappa_{ij}^{10*}\kappa_{kl}^{01}. \tag{3.25}$$

3.4 Particle Number

We focus on the neutron number N. The same principles can then be applied for proton number Z. Neutron number only has one symmetry operator $\hat{N}$, whose gauge rotations are associated with the group $U(1)_N$. With the gauge angle $\varphi_N \in [0, 2\pi]$ a group element can be represented as [8, 20]

$$\hat{R}(\varphi_N) = e^{i\varphi_N \hat{N}}. \tag{3.26}$$

As it follows from section 3.1, the neutron number projection operator is [8, 20]

$$\hat{P}^{N_0} = \frac{1}{2\pi} \int_0^{2\pi} d\varphi \, e^{i\varphi(\hat{N}-N_0)}, \tag{3.27}$$

with N_0 being the target neutron number.

An important step is to represent the rotation operator $e^{i\varphi_N \hat{N}}$ as a matrix when calculating the overlap. An HFB state is represented by the U and V matrices, where each row corresponds to a set of quantum numbers in the HO basis. Rotated U and V can be written as a function of the non-rotated ones as [10]

$$U_i^{\varphi_N} = e^{+i\varphi_N} U_i \tag{3.28}$$

$$V_i^{\varphi_N} = e^{-i\varphi_N} V_i. \tag{3.29}$$

If the rows are ordered in such a way that the top half correponds to neutrons, and the bottom half corresponds to protons, the rotation matrix can be expressed as [10]

$$R(\varphi_N) = \begin{pmatrix} e^{i\varphi_N} I_{d/2} & 0 \\ 0 & I_{d/2} \end{pmatrix}, \tag{3.30}$$

where d is the dimension of the model space. Note that the V matrix is rotated with $R^\dagger$.

Discretization of neutron number projection: In a numerical implementation of the projection operator, integrals can be discretized to evenly spaced and weighted points. One can start with performing the variable exchange

$$\varphi(n) = 2\pi \frac{n}{M_\varphi} \tag{3.31}$$

$$d\varphi = \frac{2\pi}{M_\varphi} dn \tag{3.32}$$

$$\implies n \in [0, M_\varphi], \tag{3.33}$$

where M_φ is for now an arbitrary parameter. We end up with the integral

$$\hat{P}^{N_0} = \frac{1}{M_\varphi} \int_0^{M_\varphi} dn \, e^{2\pi i \frac{n}{M_\varphi}(\hat{N}-N_0)}. \tag{3.34}$$

Since we have M_φ as a tunable parameter, we can choose this as an integer value, and take the discrete limit for $dn \to \Delta n = 1$. The discrete neutron number projection operator is [20]

$$\mathbb{P}^{N_0} = \frac{1}{M_\varphi} \sum_{n=1}^{M_\varphi} e^{2\pi i \frac{n-1}{M_\varphi}(\hat{N}-N_0)}, \tag{3.35}$$

where M_φ is now the number of points in the integral.

3.5 Spatial Symmetries

For the spatial symmetries we have four different operators. Three of these are Cartesian components of the total angular momentum operator $\hat{J}_x, \hat{J}_y, \hat{J}_z$. The fourth symmetry operator is the parity operator $\hat{\Pi}$.

The parity projection operator works differently as it is associated to a discrete symmetry. It can be written as [7]

$$P^\pi = \frac{1}{2}\left(1 + \pi\hat{\Pi}\right), \tag{3.36}$$

where $\pi \in \{-1, 1\}$ is the target parity. In this case, the rotation operator can be modeled as

$$\hat{R}_\Pi(p) = (\hat{\Pi})^p, \tag{3.37}$$

where p represents the angle 0 ($p = 0$) or 180° ($p = 1$).

For the angular momentum we have three operators and thus three angles, meaning the group element can be represented as [7, 8]

$$\hat{R}_J(\alpha, \beta, \gamma) = e^{i\alpha\hat{J}_z} e^{i\beta\hat{J}_y} e^{i\gamma\hat{J}_z}. \tag{3.38}$$

Once again we apply the same principles. The integral factor $e^{-i\Omega S_0}$ in this case is given by the Wigner functions D^J_{MK} as explained in [8, Appendix A]. This results in the angular momentum projection operator [20]

$$\hat{P}^{J_0}_{M_0K_0} = \frac{2J_0+1}{8\pi^2} \int_0^{2\pi} d\alpha \int_0^{\pi} d\beta \ \sin(\beta) \int_0^{2\pi} D^{J_0}_{M_0K_0}(\alpha, \beta, \gamma) e^{i\alpha\hat{J}_z} e^{i\beta\hat{J}_y} e^{i\gamma\hat{J}_z}. \tag{3.39}$$

The target quantum numbers are: the total angular momentum J_0, the component of the angular momentum along a fixed axis in the lab frame M_0, and the component of the angular momentum along a fixed axis in the intrinsic frame K_0 [23].

Once again, in order to calculate the overlap, the effect of the rotation operators applied to an HFB state must be handled. For the parity rotation, we need to express the effect of the parity operator $\hat{\Pi}$ in matrix notation, which is done through [7]

$$R_\Pi(p)_{kl} = \delta_{kl}\pi_k^p, \tag{3.40}$$

where π_k is the parity of the k^{th} orbital. For the full angular momentum rotation operator, we end up with the matrix also given by the Wigner functions D^J_{MK} [7]

$$R_J(\alpha,\beta,\gamma)_{kl} = D^{j_k *}_{m_k m_l}(\alpha,\beta,\gamma)\ \delta_{t_k t_l}\delta_{j_k j_l}\delta_{\pi_k \pi_l}\delta_{n_k n_l}. \tag{3.41}$$

Discretization of angular momentum projection: We start by separating the individual parts of the integral using the relations

$$\hat{R}_J(\alpha,\beta,\gamma) = \hat{R}_\alpha(\alpha)\hat{R}_\beta(\beta)\hat{R}_\gamma(\gamma) \tag{3.42}$$

$$D^{J_0}_{M_0K_0}(\alpha,\beta,\gamma) = e^{-i\alpha M_0}\ d^{J_0}_{M_0K_0}(\beta)\ e^{-i\gamma K_0}, \tag{3.43}$$

and we notice that the α and γ integrals are essentially the same. Focusing on the integral over α, we realize that it is analogous to the neutron number integral in equation (3.35), so making a similar change of basis and going to the discrete limit gives

$$\hat{\mathbb{P}}^x_{M_0} = \frac{1}{M_\alpha}\sum_{k=1}^{M_\alpha} e^{i\alpha(k)M_0}\hat{R}_\alpha(\alpha(k)), \tag{3.44}$$

and analogously for γ

$$\hat{\mathbb{P}}^z_{K} = \frac{1}{M_\gamma}\sum_{l=1}^{M_\gamma} e^{i\gamma(l)K_0}\hat{R}_\gamma(\gamma(l)), \tag{3.45}$$

where

$$\alpha(k) = \frac{1}{M_\alpha}2\pi k \tag{3.46}$$

$$\gamma(l) = \frac{1}{M_\gamma}2\pi l. \tag{3.47}$$

For the integral over β, we employ Gauss-Legendre quadrature as it is suited for this case [20]

$$\int_{-1}^{1} f(x)dx \approx \sum_{i=1}^{n} w_i f(x_i), \tag{3.48}$$

where w_i is the Gauss-Legendre weight of the i^{th} point in the integral. The β part of the integral can be expressed as

$$\hat{P}^{J_0 y}_{M_0K_0} = \frac{2J_0+1}{2}\int_0^\pi d\beta \sin(\beta)\ d^{J_0}_{M_0K_0}(\beta)\ \hat{R}_\beta(\beta), \tag{3.49}$$

and a change of variable can be performed

$$\left[\beta = \arccos(x) \rightarrow d\beta = -\frac{dx}{\sin(\beta)}\right] \tag{3.50}$$

$$\hat{P}^{J_0 y}_{M_0K_0} = -\frac{2J_0+1}{2}\int_1^{-1} dx\ d^{J_0}_{M_0K_0}(\beta(x))\ \hat{R}_\beta(\beta(x)) \tag{3.51}$$

$$= \frac{2J_0+1}{2}\int_{-1}^{1} dx\ d^{J_0}_{M_0K_0}(\beta(x))\ \hat{R}_\beta(\beta(x)). \tag{3.52}$$

Finally taking the discrete limit using Gauss-Legendre quadrature, i.e $dx \to w_n$ gives the discrete integral

$$\hat{\mathbb{P}}^{J_0 y}_{M_0 K_0} = \frac{2J_0+1}{2} \sum_{n=1}^{M_\beta} w_n \; d^{J_0}_{M_0 K_0}(\beta(x_n)) \; \hat{R}_\beta(\beta(x_n)). \tag{3.53}$$

The three operators combine into a three-dimensional sum (note that α, β, γ are now functions of the new variables) [20]

$$\hat{\mathbb{P}}^{J_0}_{M_0 K_0} = \frac{1}{M_\alpha M_\gamma} \frac{2J_0+1}{2} \sum_{k=1}^{M_\alpha} \sum_{n=1}^{M_\beta} \sum_{l=1}^{M_\gamma} w_n \, D^{J_0}_{M_0 K_0}(\alpha, \beta, \gamma) \hat{R}(\alpha, \beta, \gamma). \tag{3.54}$$

In the case of axial symmetry, the integral above reduces to [6]

$$\hat{\mathbb{P}}^{J_0} = \frac{2J_0+1}{2} \sum_{n=1}^{M_\beta} w_n \, d^{J_0}_{00}(\beta(n)) \hat{R}(0, \beta(n), 0). \tag{3.55}$$

3.6 Projected HFB - Results

The results consist of calculations of weights $|g_{S_0}|^2$ for different target quantum numbers, and symmetry-projected HFB energies. The investigated nuclei are ^{18}O, which breaks particle number symmetry, and ^{20}Ne, which breaks angular momentum symmetry. Because so few nuclei spontaneously break parity, we enforce it on ^{22}Ne in order to investigate it, instead solving the constrained HFB equations [8]. Note that the resulting energy calculation for ^{22}Ne will not be the global minimum of the unconstrained HFB equations. The model space truncation is $e_{\max} = 8$ and we use the interaction $\text{NNLO}_{\text{go}}(394)$ for all results.

Particle number and angular momentum

The weights for ^{18}O, seen in Figure 3.1, are converged at $M_\varphi = 11$. The highest weight can be found at neutron number $N_0 = 10$, which is expected since ^{18}O has 10 neutrons. Using 11 points for the integral and projecting on $N_0 = 10$ results in the energy -161.623 MeV, as seen in table 3.1. This is higher than the HFB energy without projection (-162.787 MeV), which is not necessarily a problem as in [20] we see a slight increase in energy for some cases. This increase could, however, be due to the fact that PAV is implemented instead of VAP.

For calculations based on ^{20}Ne, once again, $M_\beta = 11$ points in the integral are sufficient to get converged results for the quantities of interest. The weight seems quite low for the ground state $J = 0^+$, with the highest weight being at the excited state $J = 2^+$. This tells us that $J = 2^+$ contributes the most to the calculation. What is important is which of the contributing states gives us the lowest energy, and that is $J = 0^+$ with -197.078 MeV as seen in table 3.1. It is lower than the energy calculated with axial HF/HFB before projection (-187.698 MeV).

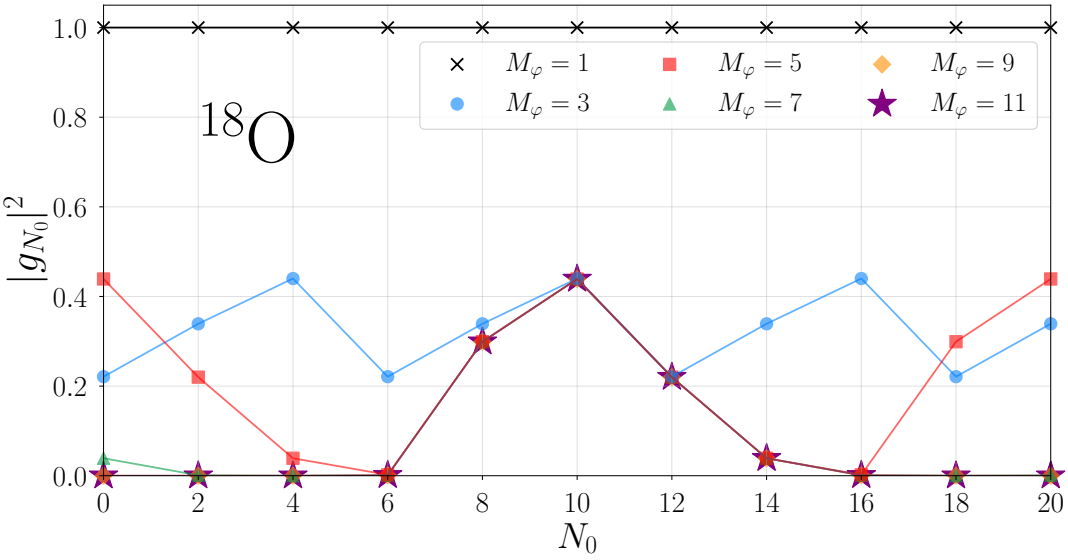

Figure 3.1: ^{18}O calculations of weights $|g_{N_0}|^2$ for different target neutron number N_0 and number of quadrature points M_φ.

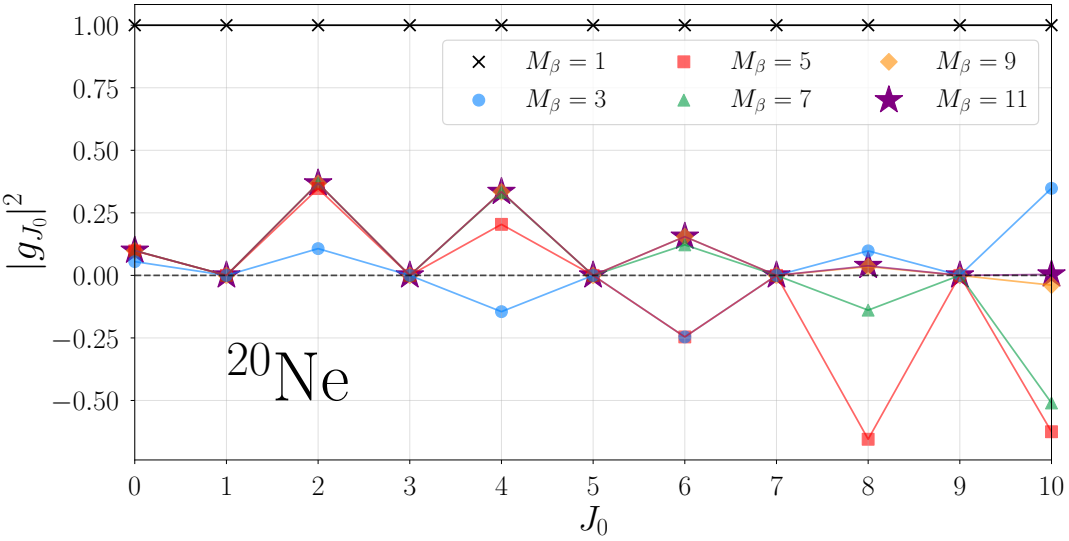

Figure 3.2: ^{20}Ne calculations of weights $|g_{J_0}|^2$ for different target total angular momentum J_0 and number of Gauss-Legendre quadrature points M_β.

Table 3.1: Ground state energy calculations for two different nuclei with different methods. Spherical (∘) HF, axial (⬭) HFB, and symmetry-projected axial (PAV ⬭) HFB.

Nucleus		^{18}O	^{20}Ne
∘ HF	[MeV]	-160.901	-176.739
⬭ HFB	[MeV]	-162.787	-187.698

Target		$N_0 = 10$	$J_0 = 0$
PAV ⬭ HFB	[MeV]	-161.623	-197.078

Parity

For ^{22}Ne, the HFB calculations were constrained with $\beta_3 = 0.1$, defined in Appendix A, which biases the solution towards an octupole deformation (parity breaking). When performing the parity projection we get a higher weight for positive parity (+) and also a lower energy ($E_+ < E_-$), shown in table 3.2. A higher weight and lower energy for positive parity is expected, as it corresponds to the physical ground state of ^{22}Ne. We also see that the energy after projection (on $\Pi_0 = +$) is lower than before the projection.

Table 3.2: Energy calculations for ^{22}Ne with enforced parity breaking. First the resulting energy with axial (⬭) HFB with enforced parity breaking, and below are the weights and energies after projection for each of the quantum numbers (+ and -).

⬭ HFB	-214.337 MeV

Target Π_0	Weight g_{Π_0}	Energy E_{Π_0}
+	0.887	-217.558 MeV
−	0.113	-189.091 MeV

4. Emulation

This chapter covers the mathematical idea behind EC, and shows how this emulation approach is implemented for an HFB solver. We once again mention the additive splitting of the Hamiltonian into a constant term H_0 and short-range interaction terms H_i [2, 6] multiplied by LECs $\mathbf{x} = \{x_i\}$

$$H(\mathbf{x}) = H_0 + \sum_{i>0} x_i H_i. \tag{4.1}$$

4.1 Eigenvector Continuation

The idea of EC is to create a reduced basis representation of a high-fidelity model [13]. Say we have an $N \times N-$dimensional parameter-dependent Hamiltonian matrix $H(\mathbf{x})$, the eigenvectors would be of dimension $1 \times N$, the full eigenvalue problem would be

$$\overbrace{\begin{bmatrix} H_{11} & H_{12} & \cdots & H_{1N} \\ H_{21} & H_{22} & \cdots & H_{2N} \\ \vdots & \vdots & \ddots & \vdots \\ H_{N1} & H_{N2} & \cdots & H_{NN} \end{bmatrix}}^{H(\mathbf{x})} \overbrace{\begin{bmatrix} v_1 \\ v_2 \\ \vdots \\ v_N \end{bmatrix}}^{\mathbf{v}} = E \overbrace{\begin{bmatrix} v_1 \\ v_2 \\ \vdots \\ v_N \end{bmatrix}}^{\mathbf{v}}. \tag{4.2}$$

To emulate the high-fidelity model, we first find a few (three is used as an example) solutions $\mathbf{a}, \mathbf{b}, \mathbf{c}$ (snapshots) generated by their corresponding parameter values $\mathbf{x}_k$, $(k = a, b, c)$

$$\begin{bmatrix} a_1 & b_1 & c_1 \\ \vdots & \vdots & \vdots \\ a_N & b_N & c_N \end{bmatrix}. \tag{4.3}$$

These snapshots are now used to create a reduced Hamiltonian matrix $H^{\mathrm{RB}}(\mathbf{x})$

$$\begin{bmatrix} a_1 & \cdots & a_N \\ b_1 & \cdots & b_N \\ c_1 & \cdots & c_N \end{bmatrix} \begin{bmatrix} H_{11} & H_{12} & \cdots & H_{1N} \\ H_{21} & H_{22} & \cdots & H_{2N} \\ \vdots & \vdots & \ddots & \vdots \\ H_{N1} & H_{N2} & \cdots & H_{NN} \end{bmatrix} \begin{bmatrix} a_1 & b_1 & c_1 \\ \vdots & \vdots & \vdots \\ a_N & b_N & c_N \end{bmatrix} = \overbrace{\begin{bmatrix} H_{aa} & H_{ab} & H_{ac} \\ H_{ba} & H_{bb} & H_{bc} \\ H_{ca} & H_{cb} & H_{cc} \end{bmatrix}}^{H^{\mathrm{RB}}(\mathbf{x})}. \tag{4.4}$$

Note that the vectors $\mathbf{a}, \mathbf{b}, \mathbf{c}$ are not orthogonal, so the eigenvalue problem must be properly normalized. We calculate the matrix of inner products N^{RB}

$$\begin{bmatrix} a_1 & \cdots & a_N \\ b_1 & \cdots & b_N \\ c_1 & \cdots & c_N \end{bmatrix} \begin{bmatrix} a_1 & b_1 & c_1 \\ \vdots & \vdots & \vdots \\ a_N & b_N & c_N \end{bmatrix} = \overbrace{\begin{bmatrix} N_{aa} & N_{ab} & N_{ac} \\ N_{ba} & N_{bb} & N_{bc} \\ N_{ca} & N_{cb} & N_{cc} \end{bmatrix}}^{N^{\mathrm{RB}}}, \tag{4.5}$$

and get the new eigenvalue problem [13]

$$\begin{bmatrix} H_{aa} & H_{ab} & H_{ac} \\ H_{ba} & H_{bb} & H_{bc} \\ H_{ca} & H_{cb} & H_{cc} \end{bmatrix} \begin{bmatrix} \widetilde{v}_1 \\ \widetilde{v}_2 \\ \widetilde{v}_3 \end{bmatrix} = \widetilde{E} \begin{bmatrix} N_{aa} & N_{ab} & N_{ac} \\ N_{ba} & N_{bb} & N_{bc} \\ N_{ca} & N_{cb} & N_{cc} \end{bmatrix} \begin{bmatrix} \widetilde{v}_1 \\ \widetilde{v}_2 \\ \widetilde{v}_3 \end{bmatrix}, \tag{4.6}$$

where $\widetilde{E}$ contains the emulated eigenvalues. The reduced Hamiltonian matrix is referred to as the Hamiltonian kernel, and the matrix of inner products is the norm kernel.

Now we apply the EC framework such that we can efficiently approximate eigenvalues and eigenvectors of the nuclear Hamiltonian at different LEC values. The reduced basis is built from a number n_{RB} of accurate ground state solutions. This time, for HF (or HFB) there is the additional complexity of the coefficient matrix (or matrices) that appears in the calculation of the Hamiltonian and norm kernels [6, 11]

$$\widetilde{N}_{\alpha\beta} = \langle \Phi_\alpha | \Phi_\beta \rangle \tag{4.7}$$

$$\widetilde{H}_{\alpha\beta}(\mathbf{x}_\odot) = \langle \Phi_\alpha | \, H(\mathbf{x}_\odot) \, | \Phi_\beta \rangle \,, \tag{4.8}$$

where $|\Phi_\alpha\rangle$ is a ground state snapshot and $\alpha = 1, 2, ..., n_{\mathrm{RB}}$. The generalized eigenvalue equation can then be solved to find the emulated ground state energy

$$\widetilde{H}(\mathbf{x}_\odot) \, |\Psi_{m,\odot}\rangle = \widetilde{E}_{m,\odot} \widetilde{N} \, |\Psi_{m,\odot}\rangle \,, \tag{4.9}$$

where m labels the spectrum and $|\Psi_{m,\odot}\rangle$ are emulated energy eigenstates made up of linear combinations of the reference snapshot states $|\Phi_\alpha\rangle$. $\widetilde{E}_{m,\odot}$ are the eigenvalues where the lowest one typically corresponds to the energy of the physical state.

In order to quickly evaluate different Hamiltonian kernels for different LEC values, the original kernel can be split up as

$$\langle \Phi_\alpha | \, H(\mathbf{x}_\odot) \, | \Phi_\beta \rangle = \langle \Phi_\alpha | \, H_0 \, | \Phi_\beta \rangle + \sum_{i>0} x_{i,\odot} \, \langle \Phi_\alpha | \, H_i \, | \Phi_\beta \rangle \tag{4.10}$$

$$= \widetilde{H}_{0,\alpha\beta} + \sum_{i>0} x_{i,\odot} \widetilde{H}_{i,\alpha\beta}. \tag{4.11}$$

For a certain set of snapshots, the set of Hamiltonian kernels $\widetilde{H}_i, i = 0, 1, ...$ only need to be calculated once. The kernels can then be used to approximate energies for many different sets of LECs $\mathbf{x}_\odot$.

4.2 Extending Emulators with Symmetry Projection

To incorporate symmetry projection, one may construct the kernels with the desired projection operator $\hat{P}^{S_0}$

$$\widetilde{N}^{S_0}_{\alpha\beta} = \langle \Phi_\alpha | \, \hat{P}^{S_0} \, | \Phi_\beta \rangle \tag{4.12}$$

$$\widetilde{H}^{S_0}_{\alpha\beta}(\mathbf{x}_\odot) = \langle \Phi_\alpha | \, H(\mathbf{x}_\odot) \hat{P}^{S_0} \, | \Phi_\beta \rangle \, . \tag{4.13}$$

Now when solving the generalized eigenvalue equation (4.9), the target (physical) eigenstate $|\Psi^{S_0}_\odot\rangle$ represents a state with preserved symmetry and quantum number S_0.

The calculation of these kernels follows the same principles as equations (3.12) and (3.13)

$$\langle \Phi_\alpha | \, \hat{P}^{S_0} \, | \Phi_\beta \rangle = \frac{1}{2\pi} \int d\Omega e^{i\Omega S_0} \, \langle \Phi_\alpha | \, \hat{R}(\Omega) \, | \Phi_\beta \rangle \tag{4.14}$$

$$\langle \Phi_\alpha | \, H_i \hat{P}^{S_0} \, | \Phi_\beta \rangle = \frac{1}{2\pi} \int d\Omega e^{i\Omega S_0} \frac{\langle \Phi_\alpha | \, H_i \hat{R} \, | \Phi_\beta \rangle}{\langle \Phi_\alpha | \, \hat{R} \, | \Phi_\beta \rangle} \, \langle \Phi_\alpha | \, \hat{R} \, | \Phi_\beta \rangle \, . \tag{4.15}$$

For the energy element, the calculation is analogous to the procedure in section 3.3, but in this case $|\Phi_0\rangle = |\Phi_\alpha\rangle$ and $|\Phi_1\rangle = \hat{R} \, |\Phi_\beta\rangle$, keeping in mind that the Hamiltonian is split in different parts.

The calculation of the rotated overlap

$$\langle \Phi_\alpha | \, \hat{R} \, | \Phi_\beta \rangle \tag{4.16}$$

becomes more complicated, explained in detail in [21]. In short, the matrix of overlaps, introduced in section 3.2, is now

$$\mathcal{O}^{\alpha\beta} = D^{\dagger\alpha}_{\text{occ}} R D^{\beta}_{\text{occ}}. \tag{4.17}$$

An example for the skew-symmetric matrix M, also introduced in section 3.2, in the case of just one pair of partially occupied orbitals in each of the states is

$$M = \begin{pmatrix} 0 & m_0^\beta & -\mathcal{O}_{\text{p}}^{\alpha\beta-1} \\ -m_0^\beta & 0 & \\ \mathcal{O}_{\text{p}}^{\alpha\beta-1} & & 0 \quad -m_0^\alpha \\ & & m_0^\alpha \quad 0 \end{pmatrix}. \tag{4.18}$$

The rotated overlap is then

$$\langle \Phi_\alpha | \, \hat{R} \, | \Phi_\beta \rangle = \sigma \ \text{pf}(M) \ \det(\mathcal{O}^{\alpha\beta}), \tag{4.19}$$

with σ as a sign factor.

4.3 Regularization

In some cases, when constructing the emulator, some snapshots could be nearly linearly dependent, leading to an ill-conditioned norm kernel [11]. To handle this, we employ a regularization method called singular value decomposition, which allows to express the norm kernel as

$$N^{\mathrm{RB}} = L\Sigma R^T, \tag{4.20}$$

with L and R being orthogonal matrices and Σ a diagonal matrix containing the singular values $s_i \geq 0$ of the norm matrix. Next, the matrices L, R and Σ are truncated so that only the columns of L and the rows of R corresponding to the k largest singular values $s > s_{\min}$ are kept. We use $s_{\min} = 10^{-8}$. Denote these new matrices as $L'_{(n_{\mathrm{RB}}\times k)}$, $R'_{(k\times n_{\mathrm{RB}})}$ and $\Sigma'_{(k\times k)}$. The reduced basis Hamiltonian is transformed as

$$\widetilde{H}'(\mathbf{x}_\odot) = \tilde{\Sigma}^{-1/2}\tilde{L}^T\widetilde{H}(\mathbf{x}_\odot)\tilde{R}\tilde{\Sigma}^{-1/2}, \tag{4.21}$$

resulting in a standard eigenvalue problem [11]

$$\widetilde{H}'(\mathbf{x}_\odot)\left|\Phi_\odot\right\rangle = \widetilde{E}'\left|\Phi_\odot\right\rangle, \tag{4.22}$$

where $\widetilde{E}'$ is now the regularized emulated energy.

As mentioned, the benefit is the handling of the ill-conditioned norm kernel, while also turning the generalized eigenvalue problem into a standard eigenvalue problem. There are however some considerations concerning the choice of snapshots. When one wishes to use emulators, the goal is to perform as few full calculations as possible. Snapshot choices that result in linear dependency means that redundant calculations have been performed. The emulation approach is computationally less costly if singular value decomposition can be avoided. Note also that a too high value of $s_{\min}$ could result in ignoring important information about the space.

4.4 Emulating HFB Ground State Energies

For all the emulation results, the only LEC being investigated is $C_{^1S_0}$. The Hamiltonian of the different solutions is constructed as

$$H(C_{^1S_0}) = H_0 + C_{^1S_0}H_1, \tag{4.23}$$

where H_1 is specifically the part corresponding to $C_{^1S_0}$, and H_0 is the part corresponding to the constant term and all other LECs. H_0 and H_1 are specified by the $\Delta\mathrm{NNLO_{go}}(394)$ interaction [18]. Note also that the vertical dashed lines in Figures 4.1, 4.3, and 4.5 correspond to the $\mathrm{NNLO_{go}}(394)$ interaction. The investigated range is $C_{^1S_0} \in [2, 4]$ using a total of 41 HFB calculations, with some being used for training and the rest as validation. The energy truncation is $e_{\max} = 8$. Also note that the neutron number projection operator had $M_\varphi = 11$ integration points.

Emulation on ^{18}O with neutron number projection:

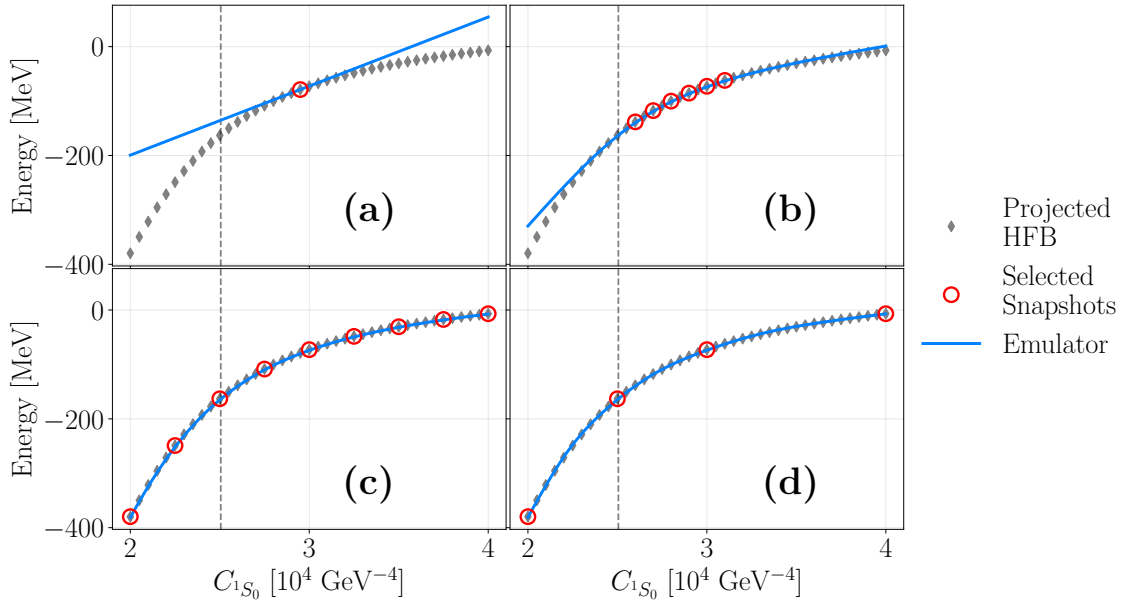

Figure 4.1: Predictions from different HFB emulators with neutron number projection on ^{18}O. **(a)** shows the result of including only one training point, it becomes a linear equation. **(b)** shows the emulator performance when including six nearby points. In segment **(c)** the emulator is using nine equidistant points in $C_{^1S_0}$ space. In **(d)** four out of the nine training points in **(c)** remain.

For the modeling of ^{18}O we use spherical HFB. As mentioned in section 3.6 this approach results in the breaking of neutron number but not proton number for this system. The kernels for the emulator that we construct include the neutron number projection operator $\hat{P}^{N_0}$ with $N_0 = 10$.

The emulator predictions shown in Figure 4.1 already exhibit noticeable extrapolation capabilities by selecting six nearby points. Perhaps more interesting is the accuracy when the chosen training points are spread out over the range. With nine training points we achieve accurate approximation over the whole investigated range. We realize though that for the higher end of the range, the energy surface does not change much. We remove some points to exercise the interpolation capabilities of the emulator. Four points, as shown in Figure 4.1.d, is sufficient to represent the whole range.

Figure 4.2 presents a quantitative evaluation of the performance of the emulator. The errors are always less than 2 MeV, with an average error of 0.74 MeV, over a 400 MeV range of outputs.

Emulation on ^{22}Ne with parity projection:

For ^{22}Ne we use axial HFB with enforced parity breaking. The result is a state that breaks angular momentum and parity. Here the kernels include the parity projection operator $\hat{P}^{\Pi_0}$ with $\Pi_0 = +1$.

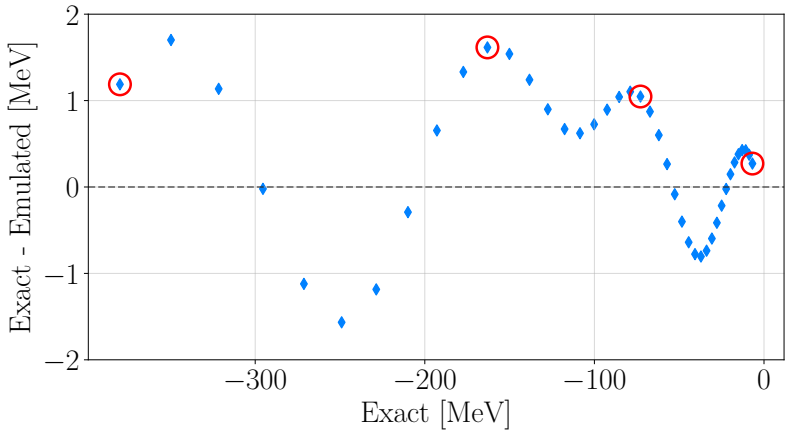

Figure 4.2: Direct comparison between the emulated energies and the neutron number projected HFB energies for ^{18}O. The red circles represent the selected training points, corresponding to Figure 4.1.d.

Predictions of different emulators with parity projection are shown in Figure 4.3. We restrict our investigation to the $C_{^1S_0}$ range that does not break particle number. Demonstrated here is also the effect of choosing two snapshots that are nearly orthogonal. This results in the emulator predictions exhibiting the behavior of separate straight lines, rather than a smooth curve. With enough points (≥ 3), the emulator can represent the output over the full range.

A quantitative investigation of the errors for the parity projected emulator is shown in Figure 4.4. Here the errors are at most ~ 2.2 MeV, with an average error of 1.3 MeV. The investigated energy output range is still roughly 400 MeV.

Emulation on ^{20}Ne with broken angular momentum:

The modeling of ^{20}Ne was performed with HFB including axially-symmetric deformations. This results in broken angular momentum and, for certain values of $C_{^1S_0}$, broken particle number. No projection operator is included in the emulator kernels. The output energies are emulated for states with broken symmetries.

In Figure 4.5, we demonstrate the extrapolation capabilities with six adjacent training points, and we also show the consequences of choosing two nearly orthogonal snapshots. In panel (d) we see the space being well represented by just a few (six) snapshots. For this efficient emulator we used a high concentration of snapshots in the low energy regime, since there is a superfluid phase transition that implies broken particle number as we lower $C_{^1S_0}$.

Once again, we investigate the errors for the emulator. Figure 4.6 again shows errors of up to ~ 2 MeV, this time with an average error of 0.75 MeV. The investigated energy range was roughly 400 MeV.

The errors of the emulators are summarized in table 4.1. We may compare this

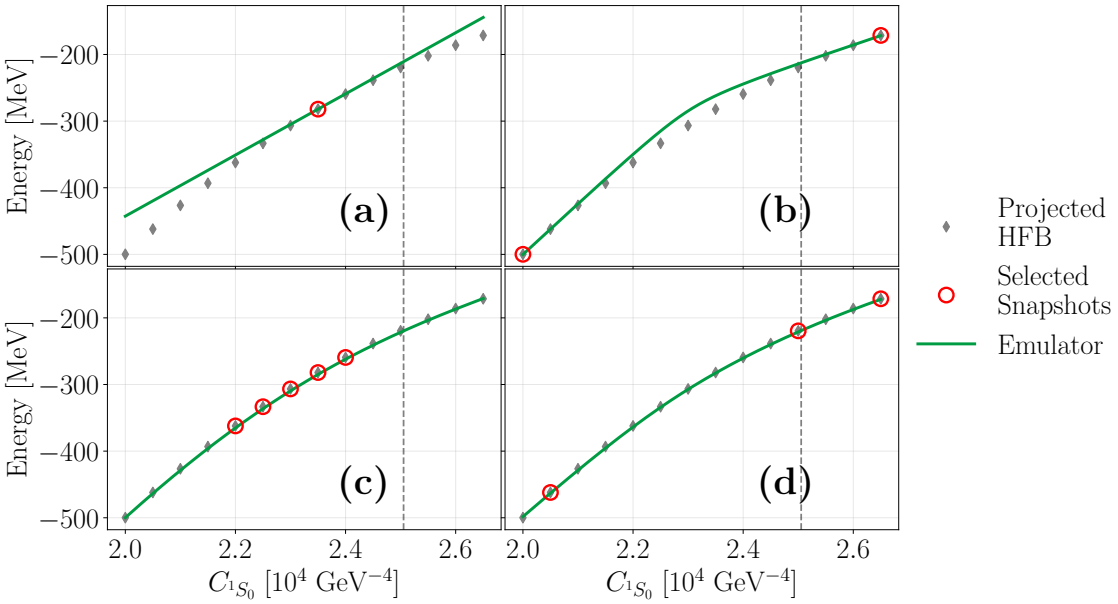

Figure 4.3: Predictions from different HFB emulators with parity projection on ^{22}Ne. **(a)** shows the result of including only one training point. **(b)** shows what happens when using two nearly orthogonal snapshots. **(c)** shows extrapolation capabilities. **(d)** is the result when including points with appropriate spacing.

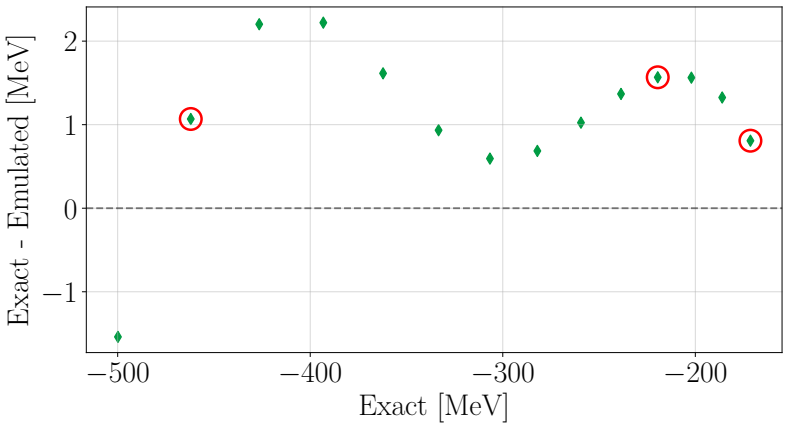

Figure 4.4: Direct comparison between the emulated energies and the parity projected HFB energies for ^{22}Ne. The red circles represent the selected training points, corresponding to Figure 4.3.d.

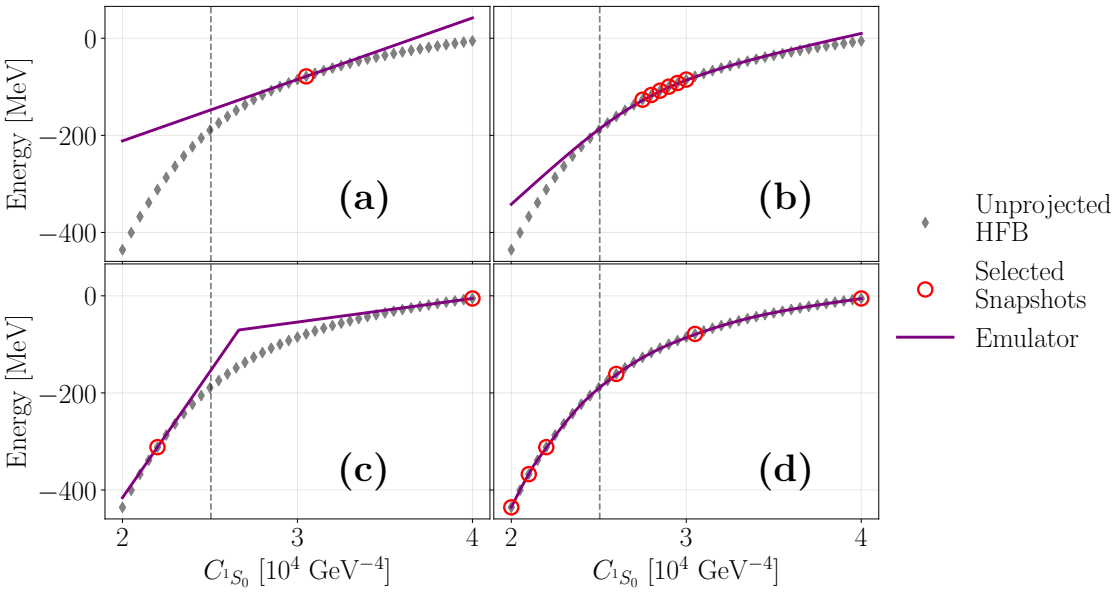

Figure 4.5: Predictions from different HFB emulators on ^{20}Ne without symmetry projection. **(a)** shows the result of including only one training point. **(b)** shows the performance when including six adjacent points. **(c)** is the result when choosing two nearly orthogonal snapshots. **(d)** showcases the interpolation capabilities.

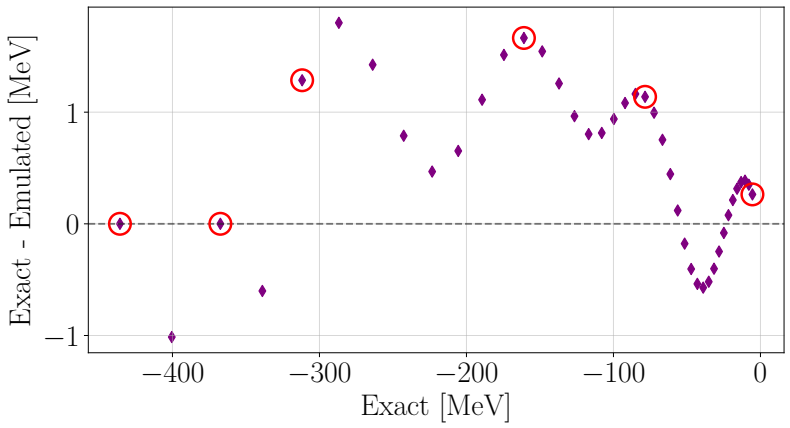

Figure 4.6: Direct comparison between the emulated energies and the HFB energies for ^{20}Ne. The red circles represent the selected training points, corresponding to Figure 4.5.d.

to results in [11], in which they construct HF emulators with ten training points. The energy landscape is simpler and the energies span from -600 MeV to -200 MeV, meaning no small magnitude energies. The relative errors reported in [11] are between 0.02% and 0.08%, which corresponds to roughly $0.1 - 0.5$ MeV. Comparing only the absolute errors, our HFB emulators has a $3 - 4$ times larger inaccuracy than the HF emulators in [11]. The less accurate result for our case is expected due to the higher complexity of HFB. Comparison with [11] serves as more of a sanity check than a benchmark. The average of the different mean-absolute errors is ≈ 0.92 MeV.

Table 4.1: Errors of the different emulators corresponding to the Figures 4.1.d, 4.3.d, and 4.5.d.

Nucleus	Mean-Absolute Error [MeV]	Maximum Error [MeV]
^{18}O	0.740	1.70
^{22}Ne	1.32	2.22
^{20}Ne	0.714	1.80

4.5 Computational Efficiency

All emulator predictions in the previous section involved 1000 evaluations. These computations were effectively instantaneous (< 0.1 s). The full HFB calculations take between 5 seconds to a few minutes for $e_{\max} = 8$, mostly dependent on the conserved symmetries. Note also that the evaluation time of the emulators is completely independent of the model space truncation, making them very favorable as we increase $e_{\max}$. Though of course, the time for calculating the snapshots and constructing the kernels is dependent on the truncation. In this section we perform a more extensive time study to give a clear idea of the efficiency. Note that the time study was made on a laptop with an i5-1335U processor.

Offline

The offline stage is separated into two parts, with the first being the time for generating snapshots. As mentioned, for the simplest case of HFB with $e_{\max} = 8$, meaning only particle number symmetry can break, a full calculation can be as quick as 5 seconds. Breaking more symmetries can lead to a full HFB calculation taking a few minutes. We call the time it takes for one full calculation T_{HFB}.

The second part of the offline stage is constructing the emulators. There are several factors that affect the offline time: model space truncation $e_{\max}$, symmetries, number of snapshots, and number of points in the projection integral. We simplify the study by only investigating spherical HFB with truncation $e_{\max} = 8$.

In the explored region of $n_{\text{RB}} < 20$, the time with respect to number of snapshots has a quadratic and a constant contribution. In Figure 4.7 a second order polynomial curve has been fitted to time measurements, resulting in

$$T_{\text{build}}(n_{\text{RB}}, M_\varphi) = \frac{97}{10^4} M_\varphi n_{\text{RB}}^2 + 2.6, \tag{4.24}$$

where T_{build} is the time to construct an emulator with M_φ points in the projection integral. In this offline time model we assumed that the constant term does not depend on the number of integral points, which is validated in Figure 4.7. The time to construct the kernels remain within the same order that it takes to perform an HFB calculation. We may add the time for generating snapshots as an offset to get

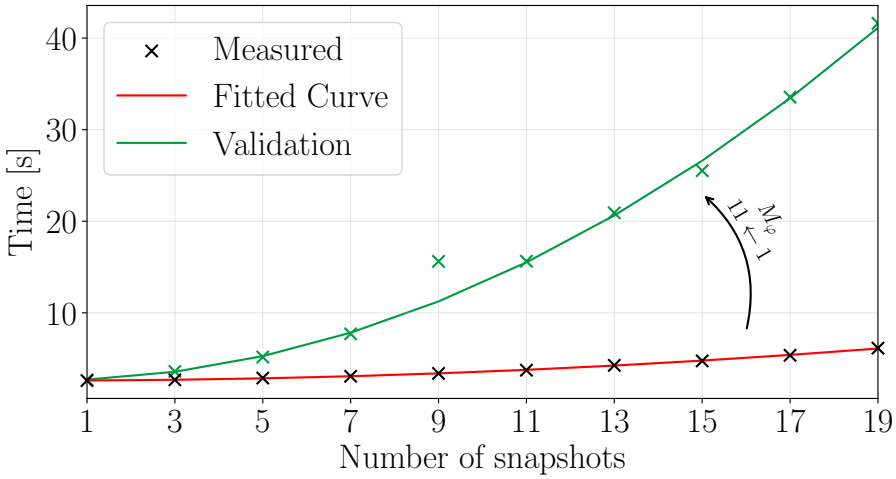

Figure 4.7: The black ×-markers are time measurements for constructing emulators without a symmetry-projection operator with the fitted red curve. The green curve is time predictions for constructing emulators including a symmetry-projection operator with 11 points in the discrete integral, along with the green markers showing the measured time.

the simple time model

$$T_{\text{off}}(n_{\text{RB}}, M_\varphi) = T_{\text{build}}(n_{\text{RB}}, M_\varphi) + n_{\text{RB}} T_{\text{HFB}}, \tag{4.25}$$

where $T_{\text{HFB}} \approx 5$ in this case.

Online

Similarly, one could model the online time; the time it takes to make predictions using emulators. In the explored regime of $n_{\text{RB}} < 20$, the time with respect to number of snapshots n_{RB} scales quadratically, along with linear and constant terms. In Figure 4.8 a second order polynomial curve has been fitted to time measurements, resulting in

$$T_{\text{on}}(n_{\text{RB}}, N_{\text{vals}}) = (3n_{\text{RB}}^2 + 18n_{\text{RB}} + 520)\frac{N_{\text{vals}}}{10^7}, \tag{4.26}$$

where T_{on} is the time the number of evaluations N_{vals} takes in seconds, assuming a perfect linear scaling with N_{vals}. Note that this time model is only reliable in the investigated n_{RB} range. We may still approximate, for example, that 10^6 evaluations with $n_{\text{RB}} = 15$ will take ~ 150 seconds. The same amount with HFB in $e_{\text{max}} = 8$ would take roughly 10^7 seconds.

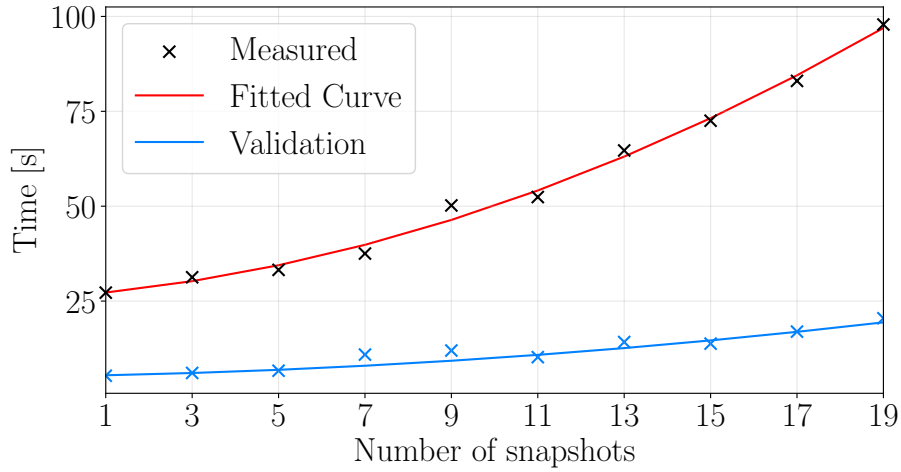

Figure 4.8: The black ×-markers are time measurements for 500 000 emulator evaluations, with the red curve fitted to these. The blue curve is time predictions for 100 000 emulator evaluations with respect to number of snapshots, along with the blue markers showing the measured time.

4.6 Structure Changes and Phase Transitions

When attempting to emulate energies, there are some considerations to keep in mind.

When performing full HFB calculations and varying the LEC, the wave function can differ greatly. Choosing snapshots that are too far away in parameter space can cause low mutual overlaps. The consequence of this is disconnected interpolation regions, demonstrated in Figures 4.3.b and 4.5.c.

A similar situation is when a phase transition occurs while varying the LEC. In such a case, the output domain typically consists of two separate regions, with the emulator requiring training points in both (and close to the phase transition) for accurate emulation. Figure 4.9 shows what the case looked like for ^{20}Ne, a phase transition to a superfluid (broken particle number) state as we decrease $C_{^1S_0}$.

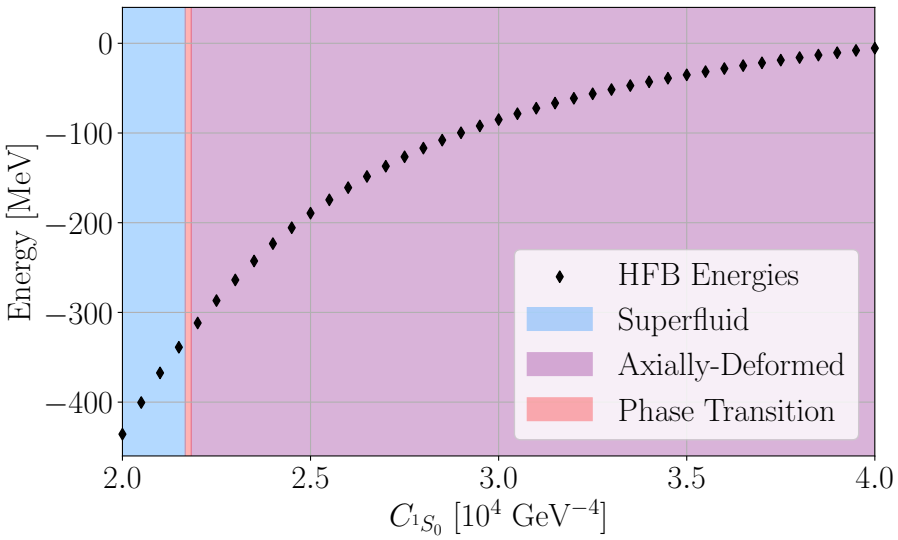

Figure 4.9: Separate regions denoting superfluid and axially-deformed states for ^{20}Ne, depending on $C_{^1S_0}$.

5. Concluding Remarks

This chapter summarizes the work performed in this project and presents the main conclusions from the emulator constructions. Possible improvements and suggestions for future work are also outlined.

5.1 Summary and Conclusions

Chapter 2 reviewed the many-body formalism underlying the mean-field description of atomic nuclei. The HF and the more general HFB methods were introduced as the approaches used in this work. By breaking different symmetries of the Hamiltonian (particle number, angular momentum, and parity symmetry), the variational space explored by the solutions of these methods was extended to able to study open-shell nuclei.

In Chapter 3 we described how the broken symmetries of the intrinsic states can be restored with projection operators. This chapter also illustrated the implementation of these operators. As a result, intrinsic states with broken symmetries were projected onto states with good particle number, angular momentum, and parity quantum numbers for the calculation of ground-state energies.

Finally, in Chapter 4, we developed emulators for HFB ground-state energies based on EC, including particle-number and parity projection. An emulator without a projection operator was also constructed for an axially-deformed nucleus. The underlying mathematical framework of EC was introduced and applied to our case. In conclusion, the constructed emulators approximated the ground-state energies with an average absolute error of 0.92 MeV across an output energy range of ~ 400 MeV using only three to six training points. Furthermore, the low computational cost was demonstrated, with an explicit example showcasing increased efficiency by five orders of magnitude compared to full HFB.

5.2 Outlook

The framework developed in this thesis could be extended to include breaking of more symmetries. Also, the projection operator for angular momentum needs to be adapted for calculation of the projected norm kernel. Additionally, the simultaneous breaking or projection of multiple symmetries remains an interesting development for future work.

The current implementation of EC selects the subspace eigenstate with the lowest

eigenvalue for a given value of the LEC. This selection rule can be unreliable for certain subspace constructions that include multiple eigensolution branches. An improvement would be to develop a selection algorithm that identifies the correct physical branch regardless of the eigenvalue.

In this project we used the symmetric formulation of EC, whereas in [11] an asymmetric formulation was used. Their results indicated that emulators with asymmetric kernels are more accurate than the symmetric variants. Implementing asymmetric EC could further improve the accuracy, and therefore calls for further investigation. The results from the symmetric formulation in [11] were used for comparison in section 4.4.

A natural extension of this work would be to include the possibility of varying different LECs in the emulator at the same time. Unlike many approaches that construct parametric models from data, EC does not require an explicit functional ansatz for the energy landscape. This makes EC potentially well-suited for higher parameter dimensions.

References

[1] B. R. Martin and G. Shaw, *Nuclear and Particle Physics: An Introduction*, 3rd ed. John Wiley & Sons, 2019, ISBN: 9781119344612.

[2] C. Mishra, A. Ekström, G. Hagen, M. Menickelly, T. Papenbrock, and S. M. Wild, *A nuclear mass model rooted in chiral effective field theory*, 2025. arXiv: 2504.20843 [nucl-th]. [Online]. Available: https://arxiv.org/abs/2504.20843.

[3] M. Wang, W. Huang, F. Kondev, G. Audi, and S. Naimi, "The ame 2020 atomic mass evaluation (ii). tables, graphs and references*," *Chinese Physics C*, vol. 45, no. 3, p. 030 003, Mar. 2021. DOI: 10.1088/1674-1137/abddaf. [Online]. Available: https://doi.org/10.1088/1674-1137/abddaf.

[4] H. Hergert, "A guided tour of ab initio nuclear many-body theory," *Frontiers in Physics*, vol. Volume 8 - 2020, 2020, ISSN: 2296-424X. DOI: 10.3389/fphy.2020.00379. [Online]. Available: https://www.frontiersin.org/journals/physics/articles/10.3389/fphy.2020.00379.

[5] B. Bally, *Nuclear charts*, https://benjaminbally.github.io/charts/, Accessed: 2026-05-04, 2025.

[6] Z. H. Sun, A. Ekström, C. Forssén, G. Hagen, G. R. Jansen, and T. Papenbrock, "Multiscale physics of atomic nuclei from first principles," *Physical Review X*, vol. 15, no. 1, Feb. 2025, ISSN: 2160-3308. DOI: 10.1103/physrevx.15.011028. [Online]. Available: http://dx.doi.org/10.1103/PhysRevX.15.011028.

[7] B. Bally and T. R. Rodríguez, "Symmetry-projected variational calculations with the numerical suite taurus: Ii. configuration mixing of symmetry-projected reference states," *The European Physical Journal A*, vol. 60, no. 3, Mar. 2024, ISSN: 1434-601X. DOI: 10.1140/epja/s10050-024-01271-0. [Online]. Available: http://dx.doi.org/10.1140/epja/s10050-024-01271-0.

[8] P. Ring and P. Schuck, *The nuclear many-body problem with 171 illustrations Peter Ring; Peter Schuck*. Springer, 1980.

[9] J. Bardeen, L. N. Cooper, and J. R. Schrieffer, "Theory of superconductivity," *Phys. Rev.*, vol. 108, pp. 1175–1204, 5 Dec. 1957. DOI: 10.1103/PhysRev.108.1175. [Online]. Available: https://link.aps.org/doi/10.1103/PhysRev.108.1175.

[10] B. Bally, A. Sánchez-Fernández, and T. R. Rodríguez, "Symmetry-projected variational calculations with the numerical suite taurus: I. variation after particle-number projection," *The European Physical Journal A*, vol. 57, no. 2, Feb. 2021, ISSN: 1434-601X. DOI: 10.1140/epja/s10050-021-00369-z. [Online]. Available: http://dx.doi.org/10.1140/epja/s10050-021-00369-z.

[11] M. C. Franzke, A. Tichai, K. Hebeler, and A. Schwenk, *Hartree-fock emulators for nuclei: Application to charge radii of ^{48,52}ca*, 2025. arXiv: 2510.08362 [nucl-th]. [Online]. Available: https://arxiv.org/abs/2510.08362.

[12] R. Machleidt and D. Entem, "Chiral effective field theory and nuclear forces," *Physics Reports*, vol. 503, no. 1, pp. 1–75, 2011, ISSN: 0370-1573. DOI: 10.1016/j.physrep.2011.02.001. [Online]. Available: http://dx.doi.org/10.1016/j.physrep.2011.02.001.

[13] T. Duguet, A. Ekström, R. J. Furnstahl, S. König, and D. Lee, "Eigenvector continuation and projection-based emulators," *Reviews of Modern Physics*, vol. 96, no. 3, Aug. 2024, ISSN: 1539-0756. DOI: 10.1103/revmodphys.96.031002. [Online]. Available: http://dx.doi.org/10.1103/RevModPhys.96.031002.

[14] F. Schwabl, *Advanced Quantum Mechanics*, 4th ed. Berlin, Heidelberg: Springer, 2008, ISBN: 978-3-540-85062-5. DOI: 10.1007/978-3-540-85062-5.

[15] J. J. Sakurai and J. Napolitano, *Modern Quantum Mechanics*, 2nd ed. Cambridge University Press, 2017.

[16] S. Binder, A. Ekström, G. Hagen, T. Papenbrock, and K. A. Wendt, "Effective field theory in the harmonic oscillator basis," *Physical Review C*, vol. 93, no. 4, Apr. 2016, ISSN: 2469-9993. DOI: 10.1103/physrevc.93.044332. [Online]. Available: http://dx.doi.org/10.1103/PhysRevC.93.044332.

[17] A. Scalesi, "On the characterization of nuclear many-body correlations in the ab initio approach," Theses, Université Paris-Saclay, Sep. 2024. [Online]. Available: https://theses.hal.science/tel-04727415.

[18] W. G. Jiang, A. Ekström, C. Forssén, G. Hagen, G. R. Jansen, and T. Papenbrock, "Accurate bulk properties of nuclei from a=2 to infinity from potentials with delta isobars," *Physical Review C*, vol. 102, no. 5, Nov. 2020, ISSN: 2469-9993. DOI: 10.1103/physrevc.102.054301. [Online]. Available: http://dx.doi.org/10.1103/PhysRevC.102.054301.

[19] D. Thouless, "Stability conditions and nuclear rotations in the hartree-fock theory," *Nuclear Physics*, vol. 21, pp. 225–232, 1960, ISSN: 0029-5582. DOI: https://doi.org/10.1016/0029-5582(60)90048-1. [Online]. Available: https://www.sciencedirect.com/science/article/pii/0029558260900481.

[20] B. Bally and M. Bender, "Projection on particle number and angular momentum: Example of triaxial bogoliubov quasiparticle states," *Physical Review C*, vol. 103, no. 2, Feb. 2021, ISSN: 2469-9993. DOI: 10.1103/physrevc.103.024315. [Online]. Available: http://dx.doi.org/10.1103/PhysRevC.103.024315.

[21] B. Avez and M. Bender, "Evaluation of overlaps between arbitrary fermionic quasiparticle vacua," *Phys. Rev. C*, vol. 85, p. 034 325, 3 Mar. 2012. DOI: 10.1103/PhysRevC.85.034325. [Online]. Available: https://link.aps.org/doi/10.1103/PhysRevC.85.034325.

[22] M. Wimmer, "Algorithm 923: Efficient numerical computation of the pfaffian for dense and banded skew-symmetric matrices," *ACM Transactions on Mathematical Software*, vol. 38, no. 4, pp. 1–17, Aug. 2012, ISSN: 1557-7295. DOI: 10.1145/2331130.2331138. [Online]. Available: http://dx.doi.org/10.1145/2331130.2331138.

[23] A. Bohr and B. Mottelson, *Nuclear Structure : (In 2 Volumes)volume I: Single-particle Motionvolume Ii: Nuclear Deformations*. World Scientific Publishing Company, 1998, ISBN: 9789813105126. [Online]. Available: https://books.google.se/books?id=NNZQDQAAQBAJ.

A. Diagnostic Parameters

There are a few different diagnostic parameters of interest in this thesis. They include the variance of the particle number $\mathrm{Var}[\hat{N}]$, the measure of quadrupole deformation (rotational symmetry breaking) β_2, and the measure of octupole deformation (parity breaking) β_3.

We start by quickly defining the particle number variance. It is defined by the standard statistical definition of variance, which gives

$$\mathrm{Var}[\hat{N}] = \langle \hat{N}^2 \rangle - \langle \hat{N} \rangle^2 . \tag{A.1}$$

The higher the variance, the more contributions from different particle number states.

Before defining the measures of deformation, we need to introduce the multipole operators. They are defined by [10]

$$Q_{lm} = \sum_{ij} \langle i | \, r^l Y_{lm} \, | j \rangle \, c_i^\dagger c_j, \tag{A.2}$$

where l is the multipole order, m is the magnetic number, $|i\rangle$ is a single-particle basis state, Y_{lm} is the spherical harmonic, and r is the radial coordinate. The multipole operators have the property

$$Q_{lm}^\dagger = (-1)^m Q_{l-m}. \tag{A.3}$$

So the hermitian average is

$$\widetilde{Q}_{lm} = \frac{1}{2}(Q_{lm} + (-1)^m Q_{l-m}). \tag{A.4}$$

Using the hermitian average of the multipole operators we may now define the measures of deformation. These measures are defined by [10]

$$\beta_{lm} = C_l \widetilde{Q}_{lm}, \tag{A.5}$$

where

$$C_l = \frac{4\pi}{3R_0^l A}. \tag{A.6}$$

Here A is the atomic mass number and $R_0 = 1.2A^{1/3}$ fm. The specific measures of mentioned in this thesis are the ones for $m = 0$, $l = 2$ (quadrupole deformation) or $l = 3$ (octupole deformation) [10]. These are $\beta_{20}(\equiv \beta_2)$ and $\beta_{30}(\equiv \beta_3)$.

B. Pfaffian

A matrix M is skew-symmetric if its negative transpose is equal to itself $M = -M^T$. The polynomial of the skew-symmetric matrix M entries is called the Pfaffian $\mathrm{Pf}(M)$. The square of the Pfaffian is the determinant [22]

$$\det(M) = \mathrm{Pf}(M)^2. \tag{B.1}$$

This is not the full definition, as the it also includes a unique choice for the sign. The Pfaffian of a $2n \times 2n$ skew-symmetric matrix (which was used in this thesis) is [22]

$$\mathrm{Pf}(M) = \frac{1}{2^n n!} \sum_{\sigma \in S_{2n}} \mathrm{sgn}(\sigma) \prod_i^n m_{\sigma(2i-1),\sigma(2i)}, \tag{B.2}$$

where $m_{k,l}$ is a matrix element of M, and S_{2n} denotes all permutations of the integers $1, \ldots, 2n$. Note that for a permutation σ, the notation $\sigma(k)$ denotes the k^{th} entry. One could calculate the Pfaffian using equation (B.2), but the computational cost scales as $\mathcal{O}(n!)$. M. Wimmer develops a polynomially scaling algorithm [22] used as a black box in this thesis.

DEPARTMENT OF PHYSICS AND ASTRONOMY
CHALMERS UNIVERSITY OF TECHNOLOGY
Gothenburg, Sweden
www.chalmers.se

CHALMERS
UNIVERSITY OF TECHNOLOGY